

USING 21CM ABSORPTION IN SMALL IMPACT PARAMETER GALAXY-QSO PAIRS TO PROBE LOW-REDSHIFT DAMPED AND SUB-DAMPED LYMAN  $\alpha$  SYSTEMS<sup>1</sup>SANCHAYEETA BORTHAKUR, TODD M. TRIPP, MIN S. YUN  
Department of Astronomy, University of Massachusetts, Amherst, MA 01003, USAEMMANUEL MOMJIAN  
National Radio Astronomy Observatory, 1003 Lopezville Road, Socorro, NM 87801, USAJOSEPH D. MEIRING<sup>2</sup>  
Department of Physics and Astronomy, University of Louisville, Louisville, KY 40292DAVID V. BOWEN  
Princeton University Observatory, Peyton Hall, Ivy Lane, Princeton NJ 08544DONALD G. YORK  
Department of Astronomy and Astrophysics, University of Chicago, Chicago, IL 60637, USA; Enrico Fermi Institute, University of Chicago, Chicago, IL 60637, USA

## ABSTRACT

To search for low-redshift damped Lyman  $\alpha$  (DLA) and sub-DLA quasar absorbers, we have conducted a 21cm absorption survey of radio-loud quasars at small impact parameters to foreground galaxies selected from the Sloan Digital Sky Survey (SDSS). Here we present the first results from this survey based on observations of SDSS J104257.58+074850.5 ( $z_{\text{QSO}} = 2.66521$ ), a quasar at an angular separation from a foreground galaxy ( $z_{\text{gal}} = 0.03321$ ) of  $2.5''$  (1.7 kpc in projection). The foreground galaxy is a low-luminosity spiral with on-going star formation ( $0.004 M_{\odot} \text{ yr}^{-1} \text{ kpc}^{-2}$ ) and a metallicity of  $-0.27 \pm 0.05$  dex. We detect 21cm absorption from the galaxy with the Green Bank Telescope (GBT), the Very Large Array (VLA), and the Very Long Baseline Array (VLBA). The absorption appears to be quiescent disk gas corotating with the galaxy and we do not find any evidence for outflowing cold neutral gas. The width of the main absorption line indicates that the gas is cold,  $T_k < 283$  K, and the H I column is surprisingly low given the impact parameter of 1.7 kpc; we find that  $N(\text{H I}) \leq 9.6 \times 10^{19} \text{ cm}^{-2}$  (GBT) and  $N(\text{H I}) \leq 1.5 \times 10^{20} \text{ cm}^{-2}$  (VLBA). VLBA marginally resolves the continuum source and the absorber, and a lower limit of  $27.1 \times 13.9$  pc is derived for the size of the absorbing cloud. In turn, this indicates a low density for a cold cloud,  $n(\text{H I}) < 3.5 \text{ cm}^{-3}$ . We hypothesize that this galaxy, which is relatively isolated, is becoming depleted in H I because it is converting its interstellar matter into stars without a replenishing source of gas, and we suggest future observations to probe this and similar galaxies.

*Subject headings:* galaxies: abundances — galaxies: ISM — quasars: absorption lines — quasars: individual (SDSS J104257.58+074850.5)

## 1. INTRODUCTION

Damped Lyman- $\alpha$  absorbers [DLAs; defined by Wolfe et al. (1986) as  $N(\text{H I}) > 2 \times 10^{20} \text{ cm}^{-2}$ ] and sub-Damped Lyman- $\alpha$  absorbers [sub-DLAs; defined by Péroux et al. (2001) as  $1.6 \times 10^{17} \text{ cm}^{-2} < N(\text{H I}) < 2 \times 10^{20} \text{ cm}^{-2}$ ] are important probes of galaxy evolution for several rea-

sons:

First, the high H I column density in DLAs shields the absorbers from photoionization by ultraviolet light, which allows the gas to cool sufficiently so that these systems can be major sites of star formation. Moreover, many studies have shown that DLAs are the dominant reservoirs of *neutral* gas throughout most of the history of the universe (e.g., Prochaska et al. 2005), and it has been suggested that DLAs are the progenitors of modern-day disk galaxies (Wolfe et al. 1986). The most recent DLA studies employing large statistical samples (Prochaska & Wolfe 2009; Noterdaeme et al. 2009a) indicate that the cosmological mass density of neutral gas in DLAs ( $\Omega_g^{\text{DLA}}$ ) decreases with redshift from  $z = 4$  down to  $z = 2.2$ , but there is controversy about how  $\Omega_g^{\text{DLA}}$  evolves at  $z \ll 2$ . The decrease in  $\Omega_g^{\text{DLA}}$  could reflect the consumption of gas by conversion to stars, but Prochaska & Wolfe (2009) argue that a more complicated picture involving both

Electronic address: sanch@astro.umass.edu

<sup>1</sup> Based on observations with (1) the telescopes of the National Radio Astronomy Observatory, a facility of the National Science Foundation operated under cooperative agreement by Associated Universities, Inc., (2) the SOAR Telescope, a joint project of Conselho Nacional de Pesquisas Científicas e Tecnológicas CNPq-Brazil, The University of North Carolina at Chapel Hill, Michigan State University, and the National Optical Astronomy Observatory, and (3) the Apache Point Observatory 3.5m telescope, which is owned and operated by the Astrophysical Research Consortium.

<sup>2</sup> Visiting astronomer, Cerro Tololo Inter-American Observatory and National Optical Astronomy Observatory, which are operated by the Association of Universities for Research in Astronomy, under contract with the National Science Foundation.

inflows and outflows is suggested by the data.

Second, the self-shielding of the DLAs facilitates accurate metallicity measurements by removing the substantial uncertainties caused by ionization corrections in lower- $N(\text{H I})$  absorption systems. In principle, DLAs do not suffer from any luminosity bias either; DLA metallicity measurements can be carried out equally well at any redshift as long as a higher- $z$  background QSO can be found. Thus, DLAs are powerful tools for tracing the chemical enrichment history of galaxies and their progenitors. The higher H I column also enables detection of weaker lines and exotic species (e.g., Prochaska et al. 2003; Junkkarinen et al. 2004; York et al. 2006a; Pettini et al. 2008; Ellison et al. 2008), and detailed signatures of various nucleosynthetic processes can be investigated in DLAs as well as those from dust extinction.

Third, by using DLAs to select high-redshift gas-rich galaxies, the kinematics of high- $z$  galactic gas flows can be investigated in detail, and with good statistical samples, based on the kinematics of sensitive metal absorption lines (Prochaska & Wolfe 1997; Prochaska et al. 2008). Several groups have used simulations and the observed DLA kinematics to argue that gravity-driven infall is not sufficient to produce the observed velocity spreads of metal lines in DLAs, and some additional process (or processes) such as galactic winds appears to be required (Razoumov et al. 2008; Pontzen et al. 2008).

However, in most cases little or no information is available regarding the *origin and environment* in which damped Lyman  $\alpha$  absorption arises, and this has hampered the exploitation of DLAs for probing galaxy evolution. Because the rest wavelength of the Lyman  $\alpha$  line is in the far ultraviolet, most DLA programs have focused on high-redshift systems ( $z \gtrsim 2$ ) that can be detected from the ground, and at those redshifts it is very challenging to study the DLA origin and environment. At low redshifts, studies have found a wide range of galaxies associated with DLAs both in terms of morphology and luminosity (Bergeron & Boisse 1991; Steidel et al. 1995; Le Brun et al. 1997; Bowen et al. 2001; Turnshek et al. 2001; Chen & Lanzetta 2003; Rao et al. 2003), but the sample of low- $z$  galaxies studied so far remains small. On the other hand, low-redshift 21 cm *emission* studies have shown that gas with  $N(\text{H I}) > 2 \times 10^{20} \text{ cm}^{-2}$  can be found in a variety of contexts (e.g., Hibbard et al. 2001) ranging from normal gas disks of high- and low-surface brightness galaxies to dynamically disturbed structures such as tidally stripped gas spurs and bridges or even detached intergalactic clouds. Galaxy interactions are expected to be more common at high redshifts, so an even larger proportion of high- $z$  DLAs could originate in disturbed structures. Interpretation of, e.g., the kinematics of DLAs, could be confusing if the samples are composed of a mixture of these different types of objects.

This raises a question: are there absorption signatures that can be used to distinguish gas in different environments such as quiescent galaxy disks vs. dynamically disturbed extraplanar structures such as tidal tails or ram-pressure detritus? All can have  $N(\text{H I}) > 2 \times 10^{20}$ , but how do their physical characteristics compare? Spectroscopic *absorption* studies of the H I 21 cm line provide unique information to address this question for several reasons: (1) In the UV/optical, QSOs are effectively point sources, but in the radio continuum, radio-loud

QSOs are often significantly extended and resolved (e.g., Lazio et al. 2009), and the absorption structure can be mapped against the extended background QSO continuum to obtain information on the spatial extent and characteristic sizes of the clouds that comprise DLAs. In addition, radio interferometers such as the Very Long Baseline Array (VLBA) can be employed to do this mapping at much higher angular resolution than is possible in other frequency bands. Thus, radio observations provide unique constraints on very small-scale structures in DLAs. Interestingly, the literature on 21cm absorber sizes suggest vastly different sizes in different environments. For example, Keeney et al. (2005) argue that the 21 cm absorption feature associated with tidal feature of NGC 3067 (Stocke et al. 1991) shows similar profile and comparable strength over a scale of 20 milli-arcsecond. The authors suggest that the feature arises in an atomic gas structure of physical size  $> 2\text{-}20 h_{70}^{-1} \text{ pc}$ . However, based on their H I emission map and photoionization model they concluded that the absorbing cloud is uniform on a scale of  $5 h_{70}^{-1} \text{ kpc}$ . It is possible that large coherent H I clouds can contain clumpy internal structures on much smaller scales. For instance, 21 cm absorbers in the Milky Way have been shown to contain much smaller structures with sizes on the order of tens of AU (e.g., Lazio et al. 2009). Although, these scales have not yet been probed in extragalactic gas clouds; the non detection of these small clouds can be attributed to the fact that they have a small volume filling factor as noted by Lazio et al. (2009). Very little information is available regarding the absorbing cloud sizes in other galaxies, which is one of the motivations for the study presented in this paper (see below). (2) The hyperfine 21 cm transition has a very low transition probability, so a substantial H I column is required to detect the line, and surveys designed to search for 21 cm absorbers in radio-loud QSOs automatically select systems that are DLAs or at least sub-DLAs. Thus, 21cm absorption reveals the kinematics and physical characteristics of the neutral gas with minimal confusion from substantially ionized gas (which can confuse analyses based on metal ions such as Si II or S II). (3) Unlike 21 cm emission, 21 cm absorption depends on the spin temperature of the gas, and combined with the high spectral resolution available with radio spectrometers, this can provide valuable constraints on the physical conditions of the absorber. (4) H I 21 cm absorption is not affected by dust and hence, such a study can address whether optical DLA studies are biased by dust extinction (see, e.g., Ellison & Lopez 2009).

For these reasons, various groups have applied 21 cm absorption spectroscopy to the study of DLAs (e.g., Kanekar & Briggs 2004; Kanekar & Chengalur 2005; Curran et al. 2007, and references therein). Unfortunately, 21 cm absorbers are rare, and blind surveys for 21 cm absorption are very inefficient with current radio telescopes, so most previous studies have searched for 21 cm absorption in known DLAs and thus are dominated by high- $z$  systems. For example, Macdonald et al. (2009) searched 243 possible sources for 21 cm absorbers with  $N(\text{H I}) > 2 \times 10^{20} \text{ cm}^{-2}$  and 3282 possible sources with  $N(\text{H I}) > 2 \times 10^{21} \text{ cm}^{-2}$  in the Arecibo Legacy Fast Arecibo L-Band Feed Array (ALFALFA) Survey. They re-detected one previously known intrinsic H I absorber, but no ad-

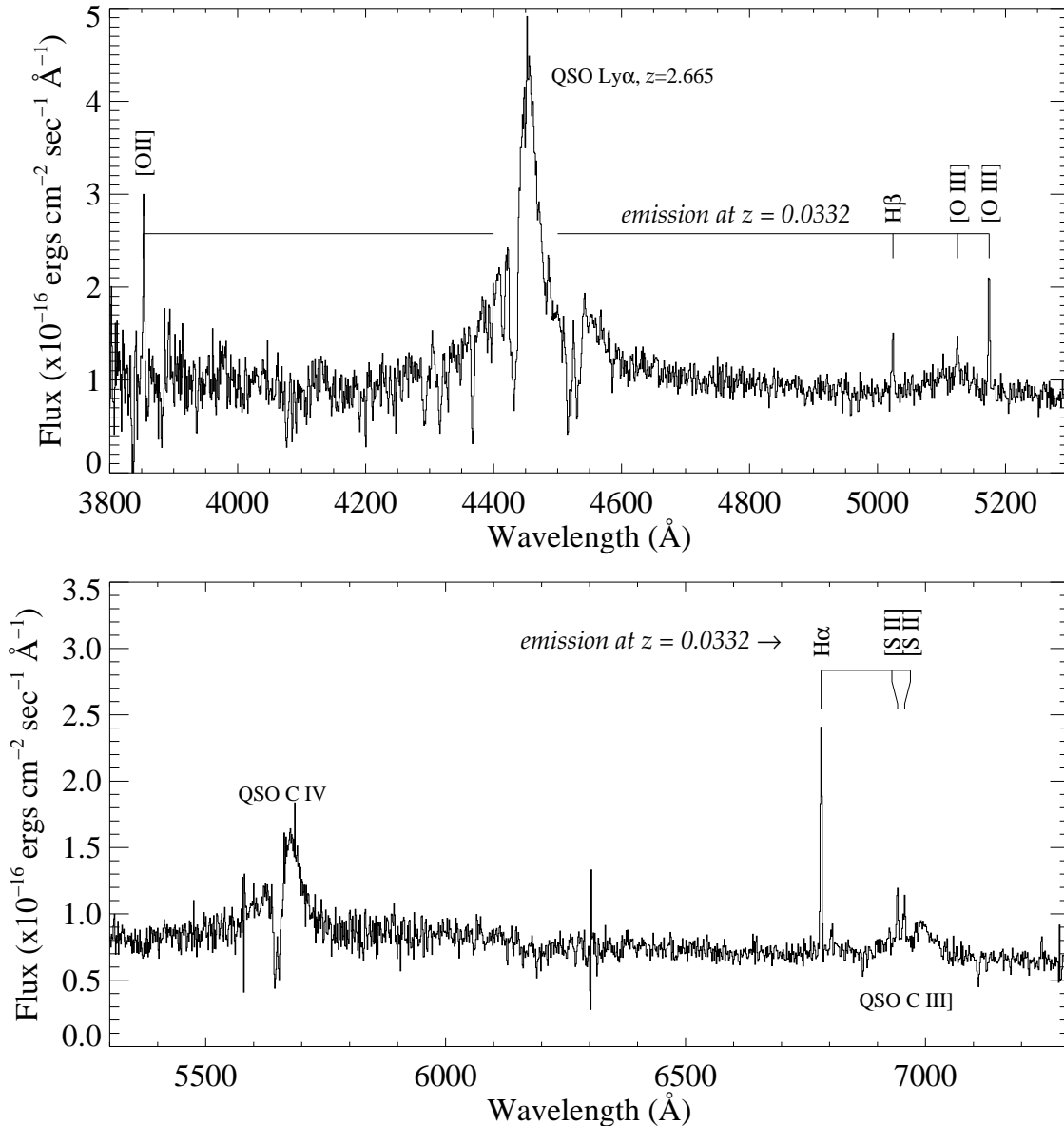


FIG. 1.— The SDSS spectrum of the  $z = 2.665$  QSO SDSS J104257.58+074850.5. While the broad Lyman  $\alpha$ , C IV and C III] emission lines are seen at the redshift of the QSO, superimposed on the spectrum are narrow emission lines of [O II], H $\beta$ , [O III], H $\alpha$  and [S II] at a redshift of  $z = 0.0332$ . The BAL nature of the QSO can be seen by the blue-shifted absorption near the QSO emission lines of C IV, N V and possibly Lyman  $\alpha$ . The complex features near 5585  $\text{\AA}$  and 6300  $\text{\AA}$  are artifacts of poor night sky subtraction.

ditional lines were identified. Likewise, searches for 21cm absorption in Mg II systems (Gupta et al. 2009; Kanekar et al. 2009a) have mostly found cases at relatively high redshifts where it is difficult to examine the environment of the absorbers.

To overcome this problem and assemble a sample of very low-redshift 21 cm absorbers suitable for environment studies, we have initiated a new survey that uses a different strategy to find the 21 cm systems. Our strategy to find low impact parameter sightlines through nearby galaxies is twofold. Firstly, we use the Sloan Digital Sky Survey (SDSS, York et al. 2000) to directly search for background QSOs at small impact parameters to low-redshift galaxies. Secondly, we search for QSO spectra

that show emission lines from *both* the QSO itself and a foreground galaxy. From this sample, we have selected radio-loud quasars based on data from the FIRST survey (Becker et al. 1995) or the NRAO Very Large Array (VLA) Sky Survey (Condon et al. 1998). The first part of our survey is to observe the radio-loud QSOs with the Green Bank Telescope (GBT) to determine if the foreground galaxy is a 21 cm absorber. Currently we are carrying out observations of 28 sight lines through 18 foreground galaxies from redshift 0.00154 to 0.2596 with projected distances varying from 1.7 to 109.7 kpc. The second part is to follow up the GBT detections with higher angular resolution observations with either the VLA or the VLBA.

In this paper we present the results of the pilot study that we conducted for this survey. This initial program successfully detected 21 cm absorption from a foreground galaxy, and we have followed up this detection with high-resolution VLBA observations and optical imaging. The paper is organized as follows. We first present the spectroscopic technique used for identifying foreground galaxies from the spectra of background QSOs (§ 2). This is followed by a detailed analysis of a QSO-galaxy pair identified using our technique and the discovery of a 21 cm absorber in the foreground galaxy. The optical imaging and foreground galaxy and environmental properties are presented in § 3, along with estimates of the foreground galaxy’s star formation rate, metallicity and stellar mass. In § 4 and § 5 we describe our radio observations and analyze the properties of the 21 cm H I absorber respectively. We discuss the physical nature and possible origin of the absorber in § 6. Finally, in § 7 we summarize our findings. Throughout the paper we use  $H_0 = 70 \text{ km s}^{-1} \text{ Mpc}^{-1}$ ,  $\Omega_m = 0.3$ , and  $\Lambda_0 = 0.7$ .

## 2. GALAXY DISCOVERY AND REDSHIFT

The presence of a galaxy close to the line of sight of the quasar SDSS J104257.58+074850.5 ( $z_{\text{QSO}} = 2.66521$ ) was discovered serendipitously by one of us (DGY) during the compilation of QSO absorption-line catalogs from the SDSS spectroscopic database (York et al. 2006b; Lundgren et al. 2009). In addition to the usual broad emission lines at  $z = 2.665$ , the SDSS spectrum of the QSO show narrow emission lines of [O II], H $\beta$ , [O III], H $\alpha$ , and [S II] at a much lower redshift. Figure 1 shows the SDSS spectrum of SDSS J104257.58+074850.5; the narrow emission lines of the foreground galaxy are readily apparent. The RA and DEC of the galaxy, which is not cataloged in SDSS, is given in Table 1. The QSO and galaxy have very similar co-ordinates of course, and to distinguish between the two in this paper, we will use the SDSS designation for the QSO, but will refer to the galaxy as “GQ1042+0747”, where GQ is an abbreviated version of “galaxy on top of QSO”. Such QSO-galaxy pairs at small impact parameters are generally not recognized as two distinct objects by the SDSS target classification algorithms. Indeed, QSO-galaxy pairs at small impact parameters are hard to find by any technique. A recent search for “composite” Sloan QSO spectra like the one shown in Figure 1 (i.e, including emission features of lower- $z$  foreground galaxies) has unearthed 21 pairs with impact parameters  $\lesssim 10 \text{ kpc}$  (Quashnock et al. 2008; Noterdaeme et al. 2009b) out of  $\approx 74,000$  QSO candidates examined. While such pairs are rare, they deserve special attention for the purpose of studying the interstellar media of the foreground galaxies.

Gaussian profile fits to the seven detected narrow (foreground) emission lines in Figure 1 give an average redshift of  $z = 0.0332 \pm 0.0001$ , with the error derived simply as the standard deviation in the seven measurements. As SDSS spectra are always corrected to heliocentric velocities, this redshift corresponds to a heliocentric velocity of  $9962 \pm 33 \text{ km s}^{-1}$ . After recognition of the composite nature of the QSO spectrum, a simple visual inspection of the SDSS images of the QSO immediately revealed a galaxy close to the QSO line of sight, confirming the notion that a galaxy was contributing light to the spectrograph fiber that had been centered on the QSO.

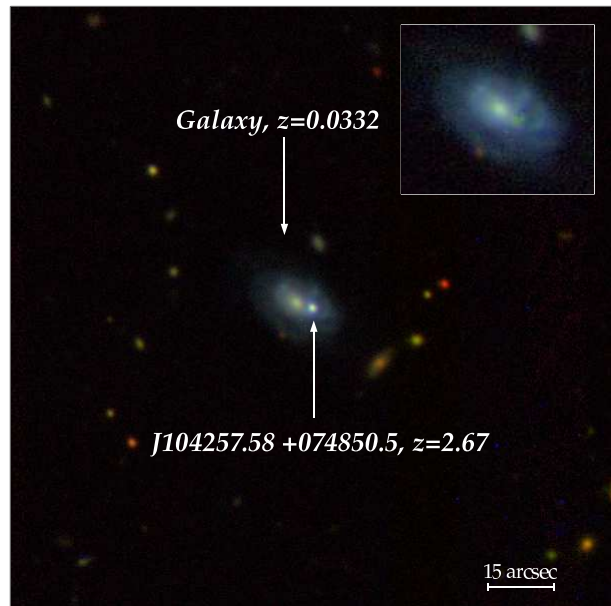


FIG. 2.— A color composite of  $g$ -,  $r$ - and  $i$ -band images of the field around SDSS J104257.58+074850.5 taken with the SOAR telescope. NE is to the top left of the image, and the scale is indicated bottom-right. The inset shows the galaxy after subtraction of the QSO profile.

As part of a follow-up investigation to search for interstellar Ca II and Na I absorption lines arising from gas in the foreground galaxy, we observed the QSO using the Dual Imaging Spectrograph (DIS) on the Astrophysical Research Consortium (ARC) 3.5 m telescope at the Apache Point Observatory (APO) on 06 January 2006. The DIS was configured with the high-resolution gratings and a 0.9 arcsec slit, giving a spectral resolution of  $\approx 80 \text{ km s}^{-1}$  (FWHM) at 6700 Å. Although conditions were too poor to obtain spectra with sufficient S/N to detect absorption lines from the foreground galaxy, the H $\alpha$  emission line was detected, permitting an independent measurement of the galaxy’s redshift, at a resolving power of about twice that of the SDSS data. We extracted spectra over a 5 arcsec aperture centered on the QSO and tied the zero-point of the wavelength calibration to four narrow skylines which were also covered by the observations. From the H $\alpha$  line alone, we measured a redshift of  $z = 0.03321 \pm 0.00003$ , with the error derived from the standard deviation in the set of differences between the rest wavelengths of the four sky lines and the wavelengths we measured. After correcting the observed radial velocity to a heliocentric one, we found that the H $\alpha$  emission line gave a systemic velocity of  $9932 \pm 10 \text{ km s}^{-1}$ .

## 3. OPTICAL PROPERTIES AND ENVIRONMENT OF THE FOREGROUND GALAXY

### 3.1. SOAR Optical Imaging

Although the galaxy is clearly visible in SDSS images, little can be inferred from the SDSS photometry due to the blending of the galaxy’s image with that of the QSO. To learn more about the nature of the foreground galaxy, we obtained deeper images with better angular resolution using the SOAR Optical Imager (SOI, Schwarz et al. 2004) on the 4.1 m Southern Astrophysical Research (SOAR) telescope at Cerro Pachón in Chile. Exposures were made using  $g$ -,  $r$ -, and  $i$ -band filters for 10, 30,

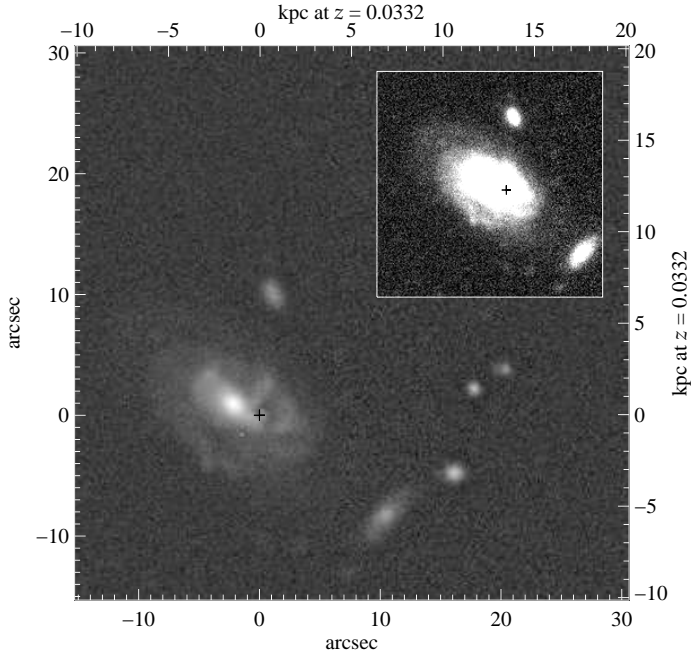


FIG. 3.— Grayscale representation of the  $r$ -band image of the galaxy GQ1042+0747 in front of SDSS J104257.58+074850.5. The QSO profile has been removed, although its original position is labelled with a cross, and the image has been processed with a gentle unsharp mask. *Inset*: The same image of the galaxy reproduced using a much harder stretch in order to show the outer spiral arm to the NE of the galaxy. The position of the QSO prior to removal is again marked with a cross.

and 15 minutes, on 2 March, 28 February, and 1 March 2009, respectively. The data were processed in the conventional way, and calibrated astrometrically using the SCAMP software package (Bertin 2006). Individual frames were co-added using the SWARP software (Bertin et al 2002), which resamples and co-adds the individual images with the derived astrometric solution based on SDSS astrometry. The final coadded  $g$ -,  $r$ - and  $i$ -band images had resolutions of 1.2, 0.7 and 0.8 arcsec FWHM, respectively. These were assembled into a color image following the prescription given by Lupton et al. (2004), using the data at the original resolutions, and applying an inverse hyperbolic sine (*asinh*) scaling algorithm. The resulting multicolor image of the QSO-galaxy pair is shown in Figure 2.

### 3.2. Photometry and Surface-Brightness Profile

To derive accurate measurements for the physical parameters of GQ1042+0747, we constructed a Point Spread Function (PSF) from a 2-D Moffat profile fit to stellar images in each of the  $g$ -,  $r$ -, and  $i$ -band images, and subtracted a suitably scaled PSF from the QSO profile. The galaxy, with the QSO profile removed, and again formed from a co-addition of all three colors, is shown inset in Figure 2.

A more detailed representation of the galaxy in the  $r$ -band image is shown in Figure 3. To better highlight the small-scale structure in the galaxy, we used the technique of unsharp masking, using the procedure outlined in Jenkins et al. (2005). We found that “gentle” unsharp masking using a Gaussian with width  $\sigma = 5$  pixels most

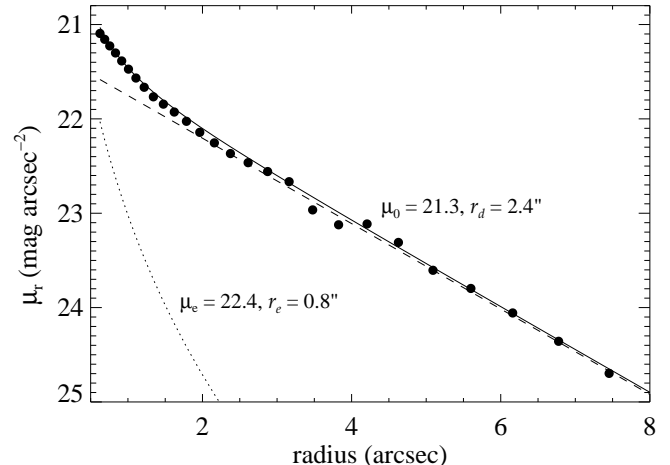


FIG. 4.— The  $r$ -band surface brightness profile of the galaxy in front of SDSS J104257.58+074850.5. The black dots are data points obtained using the IRAF isophote package. The final fit (solid line) is the result of co-adding an exponential disk profile (dashed line) and an  $r^{1/4}$  profile (dotted line). The relevant parameters for each model are given alongside the profiles.

effectively enhanced the low-level morphological features of the galaxy. In Figure 3, this unsharp mask image is shown, again scaled using the *asinh* scaling algorithm. The image shows that the galaxy is an inclined spiral, perhaps with a bar at its center. Some evidence of spiral arms can be seen to the SW of the center (below and to the right of the QSO’s position). A much harder stretch of the original image (the non unsharp mask data), shown inset in Figure 3, clearly reveals an outer spiral arm to the NE of the galaxy (top left of the inset). The main image in Figure 3 also shows a ‘plume’, some 2 – 3 arcsec directly above the position of the QSO, which is not an artifact of the QSO profile subtraction. Determining whether this is simply part of the normal spiral pattern of a galaxy, or, perhaps related to what might be a companion dwarf galaxy, SDSS J104257.52+074900.5,  $\sim 10$  arcsec due north of the QSO’s position, will require higher resolution data. The companion dwarf galaxy has magnitudes measured from the SOAR data of  $g = 22.1$ ,  $r = 21.5$  and  $i = 21.2$ , with errors of 0.1 mags.

With these images, we were able to measure the galaxy properties listed in Table 1. The magnitudes of the galaxy and its major-to-minor axis ratio were derived using the *sExtractor* software package (Bertin & Arnouts 1996); the extinction from dust in the Milky Way was taken from the maps of Schlegel et al. (1998), and these values were used to correct the absolute magnitudes (although no  $k$ -correction was applied).

To derive a surface brightness profile, we used the *ellipse* routines in the STSDAS package *isophote* (Jedrzejewski 1987) to fit the  $r$ -band data. The results are shown in Figure 4. The profile is that observed along the semi-major axis — no other corrections have been applied, and no attempt was made to first deconvolve the data using the PSF. As Figure 4 shows, more than a simple exponential disk model is required to explain the data, so we fit a combination of a disk model with a classical  $r^{1/4}$  profile. When the intensity profile of a galaxy is converted to surface brightness,  $\mu$ , the profiles

TABLE 1  
 PROPERTIES OF GQ1042+0747, THE FOREGROUND GALAXY IN THE QSO-GALAXY PAIR

Center RA and DEC	10:42:57.74 +07:47:51.3
Redshift $z_{\text{gal}}$	$0.03321 \pm 0.00003^a$ , $cz = 9932 \pm 10 \text{ km s}^{-1}$
Impact parameter	$2.5'' \equiv 1.7 \text{ kpc}$ at $z_{\text{gal}}$
Magnitudes <sup>b</sup>	$g = 18.59$ , $r = 18.05$ , $i = 18.08$
MW extinction	$g = 0.12$ , $r = 0.08$ , $i = 0.06$
Absolute magnitudes <sup>c</sup>	$M_g = -17.35$ , $M_r = -17.85$ , $M_i = -17.80$
Major/Minor axis ratio	1.55
Inclination <sup>d</sup>	50 degrees
Surface Brightness ( $r$ -band)	$\mu_o = 21.3$ , $r_d = 2.4''$ ; $\mu_e = 22.4$ , $r_e = 0.8''$
Log Metallicity	$-0.27 \pm 0.05$ (N2 index); $-0.32 \pm 0.03$ (O3N2 index)

<sup>a</sup> Redshift is from APO spectrum of H $\alpha$  line.

<sup>b</sup> Isophotal magnitudes from `sExtractor`. Formal errors on these values are  $\pm 0.02$  mags.

<sup>c</sup> Corrected for Milky Way extinction, but no k-correction applied.

<sup>d</sup>  $\cos^{-1}(b/a)$ , where  $a$  and  $b$  are the major and minor isophotal axes.

are given by:

$$\mu_1 = \mu_e + 8.325 \left[ \left( \frac{r}{r_e} \right)^{1/4} - 1 \right] \quad (1)$$

$$\mu_2 = \mu_o + 1.086 \frac{r}{r_d} \quad (2)$$

where  $r_e$  and  $r_d$  are the scale lengths of the bulge and disk components respectively, and  $\mu_e$  and  $\mu_o$  are the surface brightness values at those radii. We fitted a combination of these theoretical profiles to the observed values of  $\mu$  by minimizing the value of  $\chi^2$  between the fit and the data, and derived the values listed in Table 1. The resulting fit is shown in Figure 4.

### 3.3. Star-Formation Rate, Metallicity, and Stellar Mass

GQ1042+0747 is a low luminosity spiral with  $L = 0.048 L_\star$  in the  $r$ -band (using  $M_r^\star = -21.2$  from Table 2 of Blanton et al. 2003). Emission-line measurements from the SDSS spectrum of the foreground galaxy are presented in Table 2. The 3 arcsec-diameter fiber used to make these measurements was centered at the QSO's position. Most of the observed region covered the disk; some parts of the central region of the foreground galaxy were also captured. We estimated the star formation rate (SFR) from the H $\alpha$  (Kennicutt 1998) and O[II] transitions (Kewley et al. 2004) using the following relationships,

$$\text{SFR}(\text{H}\alpha) = 7.9 \times 10^{-42} \times \text{L}(\text{H}\alpha, \text{ergs s}^{-1}) M_\odot \text{ yr}^{-1} \quad (3)$$

$$\text{SFR}(\text{O}[\text{II}]) = 6.58 \times 10^{-42} \times \text{L}(\text{O}[\text{II}], \text{ergs s}^{-1}) M_\odot \text{ yr}^{-1} \quad (4)$$

The SFR was found to be  $1.26 \times 10^{-2}$  and  $8.6 \times 10^{-3} M_\odot \text{ yr}^{-1}$  using equation 3 and 4 respectively, over an area of  $3.1 \text{ kpc}^2$  in the rest frame of the GQ1042+0747. This corresponds to SFR surface density of  $4.1 \times 10^{-3}$  and  $2.8 \times 10^{-3} M_\odot \text{ yr}^{-1} \text{ kpc}^{-2}$ , respectively. The Balmer decrement,  $I$  ( $\text{H}\alpha/\text{H}\beta$ ) =  $3.0 \pm 0.4$  suggests a low dust content in this galaxy. The metallicity of the galaxy estimated using the N2 index (Pettini & Pagel 2004) is  $\log(\text{O}/\text{H}) + 12 = 8.42 \pm 0.05$ . Assuming a solar abundance of  $\log(\text{O}/\text{H}_\odot) = 8.69$  (Asplund et al. 2009), the logarithmic measured metallicity is then  $-0.27 \pm 0.05$  dex relative to solar. The O3N2 index yielded a similar metallicity of  $-0.32 \pm 0.03$  dex relative to solar.

It is now well-known that galaxies in the nearby universe follow mass-metallicity and luminosity-metallicity relationships (e.g., Tremonti et al. 2004). It is often argued that the mass-metallicity trend has important implications regarding galactic outflows, so it is of interest to consider where GQ1042+0747 is located in the mass-metallicity trend. Referring to Figure 5 in Tremonti et al. (2004), we see that GQ1042+0747 is a relatively low-luminosity galaxy and has a somewhat low metallicity compared to other SDSS galaxies of comparable absolute magnitude, but given the scatter in the relationship, the observed luminosity and metallicity of GQ1042+0747 are in good agreement with the usual luminosity-metallicity trend. To estimate the stellar mass of the galaxy, we use equation 1 of McIntosh et al. (2008), which is based on the stellar  $M/L$  ratios from Bell et al. (2003), and we obtain

$$\log \left( \frac{M_{\text{stars}}}{M_\odot} \right) \approx 9.1. \quad (5)$$

Thus, the metallicity is low for its stellar mass [see Figure 6 in Tremonti et al. (2004)], but again GQ1042+0747 follows the general trend within the observed scatter. We will discuss the implications of the mass and metallicity of the galaxy compared to its absorption properties in § 6.

### 3.4. Large-Scale Environment of GQ1042+0747

A benefit of using SDSS to select low- $z$  galaxy-QSO pairs is that SDSS provides detailed information about the global context of the galaxy and its affiliated absorption. We will show below that despite the fact that GQ1042+0747 is clearly a star-forming spiral galaxy, it has a surprisingly low H I column density in its inner disk, and overall it has a low H I mass. The cause for its H I deficiency is an interesting question, and we will hypothesize that this is related to the galaxy's environment. To set the stage for this discussion, we show the large-scale distribution of SDSS galaxies near GQ1042+0747 in Figures 5 and 6. Figure 5 shows the distribution of SDSS galaxies versus redshift along the line of sight to SDSS J104257.58+074850.5 out to  $z = 0.053$ ; the panels show the overall (absolute) projected distance of the galaxies from the sight line (upper panel) and the projected distance in the right ascension and declination directions only (middle and lower panels, respectively). This is a cylinder cut from SDSS spectroscopic data (up to DR7) centered on the QSO. SDSS is a magnitude-



TABLE 2  
 FOREGROUND-GALAXY EMISSION-LINE MEASUREMENTS AND IMPLIED STAR-FORMATION RATES

Line <sup>a</sup>	$EW_r$ (Å)	$I_r$ ( $\times 10^{-16}$ ergs $\text{cm}^{-2}$ $\text{s}^{-1}$ )	$L_r$ ( $\times 10^{39}$ ergs $\text{s}^{-1}$ )	SFR surface density ( $M_\odot \text{ yr}^{-1} \text{ kpc}^{-2}$ )
H $\alpha$ . . . . .	$8.8 \pm 0.3$	$6.7 \pm 0.2$	$1.6 \pm 0.06$	0.0041
[O II] . . . . .	$5.1 \pm 0.6$	$5.3 \pm 0.6$	$1.3 \pm 0.2$	0.0028
H $\beta$ . . . . .	$2.5 \pm 0.4$	$2.2 \pm 0.3$	$0.56 \pm 0.08$	n/a
[N II] $\lambda$ 6585 . . . . .	$1.3 \pm 0.3$	$0.96 \pm 0.18$	$0.24 \pm 0.06$	n/a
[O III] $\lambda$ 5008 . . . . .	$4.7 \pm 0.3$	$4.1 \pm 0.3$	$1.0 \pm 0.07$	n/a
[O III] $\lambda$ 4960 . . . . .	$1.5 \pm 0.3$	$1.6 \pm 0.3$	$0.4 \pm 0.07$	n/a

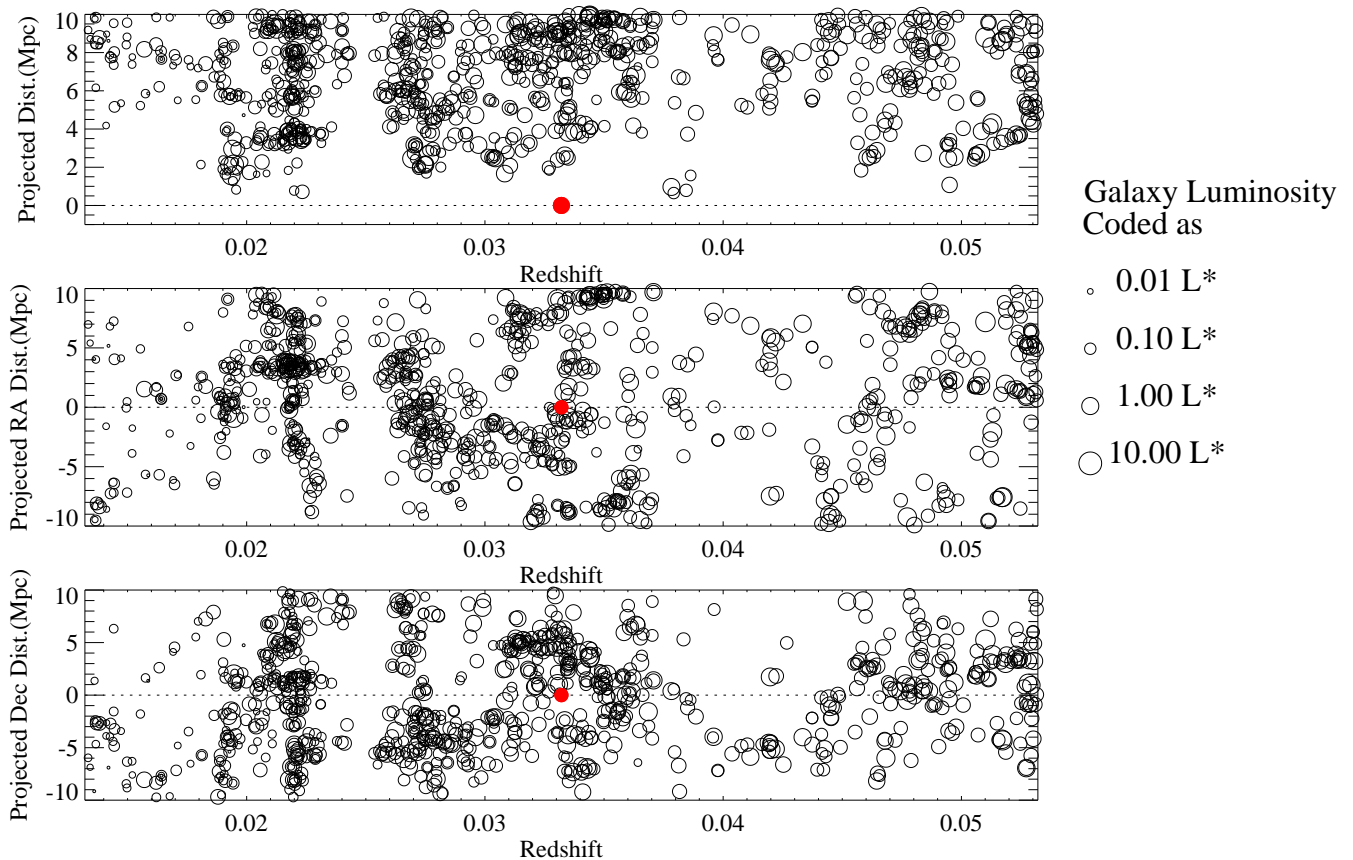
<sup>a</sup>Vacuum wavelength


FIG. 5.— Projected distance of SDSS spectroscopic galaxies in the field of SDSS J104257.58+074850.5. The sight line to the QSO is indicated with a dashed line, and galaxies are plotted with open circles with size indicating the galaxy luminosity according to the legend at the right. GQ1042+0747 is plotted with a large red circle. *Top*: Absolute projected distance from the sight line. *Middle*: Projected distance in the RA direction. *Bottom*: Projected distance in the declination direction. It is evident that the galaxy is relatively isolated and the nearest galaxy is  $\sim 2$  Mpc away. The galaxy can be considered as a field galaxy although it lies at the edge of a large-scale structure filament.

limited survey, so the galaxy points are plotted with symbol sizes that indicate the object’s luminosity based on values from NYU Value Added Catalog (Blanton et al. 2005), as shown in the legend, to give the reader a sense of the survey completeness for various galaxy luminosities. GQ1042+0747 is shown with a large red dot. We show a substantial range in redshift so that voids and large-scale structures in the galaxy distribution can be visually recognized. In order to zoom in on the more immediate vicinity of GQ1042+0747, Figure 6 shows the RA and Dec of only galaxies with redshifts within  $\pm 240$   $\text{km s}^{-1}$  of GQ1042+0747. In this figure, the symbol color indicates the velocity difference between the galaxy redshift and the redshift of the 21cm absorption detected in

GQ1042+0747 (§ 4), and the symbol size indicates the galaxy luminosity, as reflected in the figure legend.

From Figures 5 and 6, we notice the following aspects of the GQ1042+0747 environment: (1) The galaxy is located near the boundary of a large-scale structure and most likely in a low density region. This is readily apparent in Figure 6 — there is a paucity of galaxies southeast of GQ1042+0747, but many galaxies are found to the northwest with a prominent galaxy group apparent at  $\text{RA} \approx 157^\circ$  and  $\text{Dec} \approx 13^\circ$ . (2) Qualitatively, GQ1042+0747 appears to be located within the boundaries of the large-scale structure, but nevertheless it appears to be relatively isolated — the nearest neighbor galaxy is  $> 1.8$  Mpc away in projection and

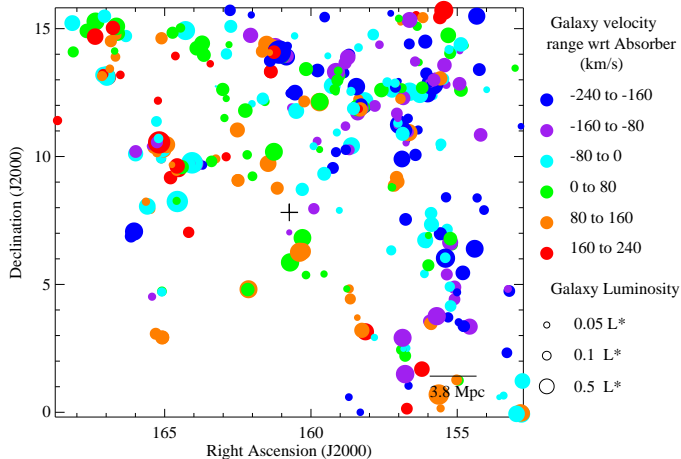


FIG. 6.— Distribution of SDSS galaxies (filled circles) near the SDSS J104257.58+074850.5 sight line (plus symbol) in Right Ascension and Declination. Following the legend at upper right, the colors of the circles indicate the velocity difference between the galaxy and the centroid of the 21cm absorption detected in GQ1042+0747, ranging from  $v_{\text{galaxy}} - v_{21\text{cm}} = -240$  to  $+240$  km  $\text{s}^{-1}$ . The circle size represents the galaxy luminosity as shown in the lower right key. The plot clearly shows a density gradient between the northwestern and the southeastern side of GQ1042+0747 confirming that it relatively isolated galaxy at the edge of a large scale structure filament.

is offset in velocity, so the three-dimensional nearest-neighbor distance could be significantly larger. Traditionally, GQ1042+0747 would be considered a “field” galaxy; in more recent nomenclature, the galaxy might be referred to as a “wall” galaxy. A detailed spectroscopic study of the immediate environments of this galaxy would help to clarify how isolated it is. We believe that the relative isolation may have been an important factor that has affected this galaxy’s evolution, as we will discuss in § 6.

#### 4. 21 CM ABSORPTION SPECTROSCOPY

To search for 21 cm absorption from the ISM/halo of the foreground galaxy, SDSS J104257.58 + 074850.5 was observed with three complementary National Radio Astronomy Observatory (NRAO) telescopes: the 100 meter GBT, the VLA in the B configuration, and the VLBA. The optical redshift of GQ1042+0747 was used to choose the bandpasses for the 21 cm observations. To maximize the effectiveness of our search for 21 cm absorption in the general vicinity of the foreground galaxy, the VLA was setup to provide the broadest spectral coverage that could be afforded at a reasonable spectral resolution. This resulted in sub-optimal spectral resolution for the VLA ( $10.6$  km  $\text{s}^{-1}$ ), but was overcome by the excellent resolution of the GBT ( $0.33$  km  $\text{s}^{-1}$ ). Following the detection of the absorber, VLBA H I observations were then carried out centered at the redshift of the absorber. Spectral resolution of  $0.9$  km  $\text{s}^{-1}$  was achieved in our VLBA observations along with a superb milli-arcsecond (mas) spatial resolution of  $22$  mas  $\times$   $9$  mas.

##### 4.1. Green Bank Telescope Observations

We observed SDSS J104257.58+074850.5 with the GBT for a total on-source integration time of nearly 85 minutes over two sessions on 5-6 August 2006 as part of program GBT06B-052. The source was observed in

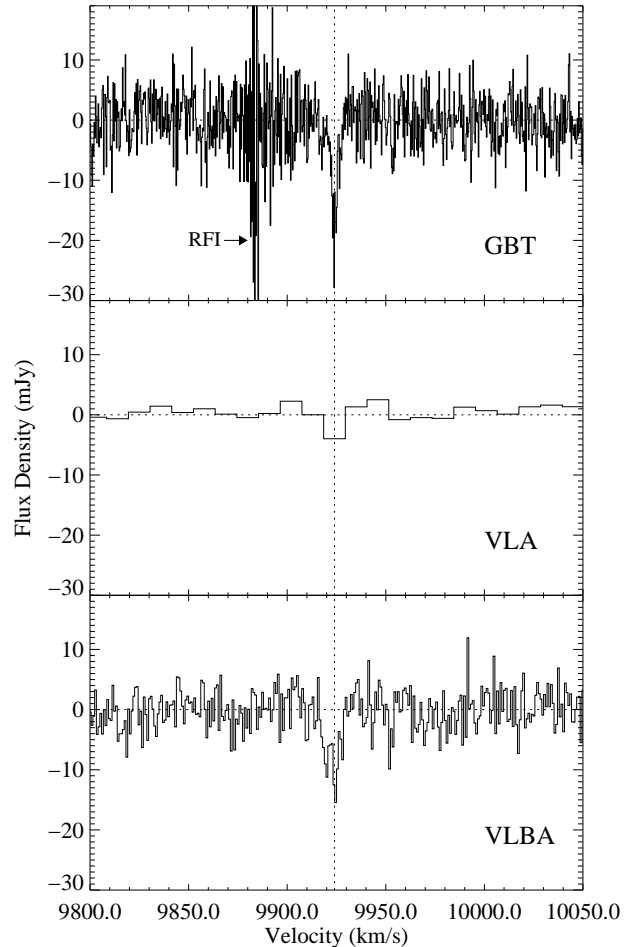


FIG. 7.— Continuum-subtracted GBT, VLA, and VLBA spectra of SDSS J104257.58+074850.5 covering the velocity range of redshifted 21 cm absorption associated with the foreground galaxy. The VLBA spectrum is extracted from pixels with more than  $400$   $\mu\text{Jy}$  (i.e.  $5\sigma$ ) continuum flux. The vertical dotted line marks a significant absorption feature that is evident in all the three spectra at  $9924$  km  $\text{s}^{-1}$ . An expanded plot of the 21 cm absorption profile in the GBT data and its comparison with VLBA data is shown in Figure 8.

two frequencies corresponding to the H I 21 cm and OH 18 cm transitions at the redshift of the foreground galaxy. Unfortunately, the OH data were corrupted by severe interference and were rendered unusable, so hereafter we only discuss the 21 cm data. We used the dual polarization L-band system with a bandwidth of  $12.5$  MHz. Nine-level sampling and two IF settings were employed to provide  $8196$  channels with  $1.56$  kHz ( $0.33$  km  $\text{s}^{-1}$ ) per channel, covering a total velocity range of  $2800$  km  $\text{s}^{-1}$ . The source 3C 286 was used as the flux density calibrator, and a calibration of  $1.65 \pm 0.05$  K/Jy was determined from the mean of the four independent recordings. The observation was carried out in standard position switching scheme by cycling through the ON-OFF sequence, dwelling for 300 seconds at each position. Data was recorded every 30 seconds to minimize the affect of radio frequency interference (RFI). A position offset of  $+20'$  in Right Ascension was adopted for the OFF position so that presence of any confusing sources in the OFF position could be tracked. The H I data showed slight sinusoidal baseline modulation on scales of  $\approx 1000$  km  $\text{s}^{-1}$



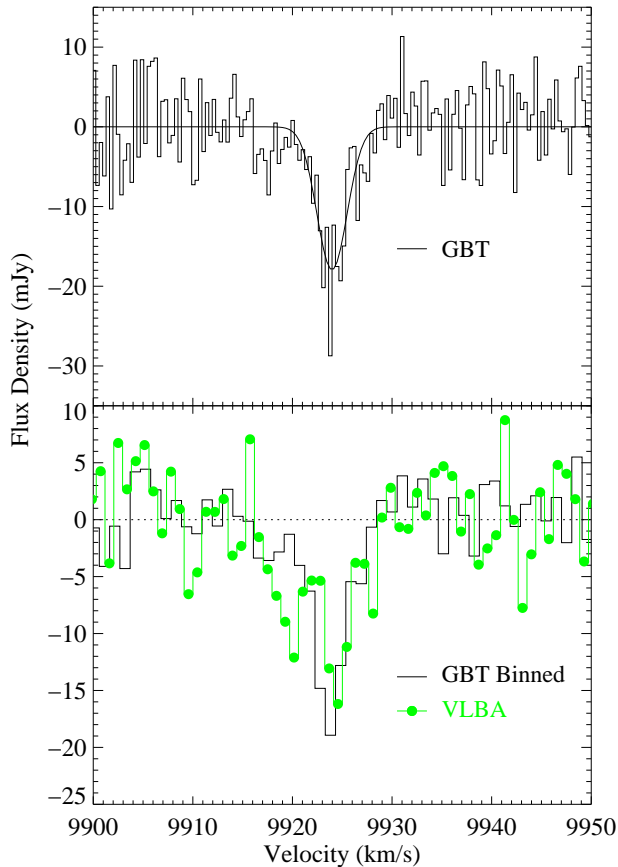


FIG. 8.— *Top*: The continuum-normalized GBT spectrum of the 21 cm absorption detected at  $9923.97 \pm 0.17$  km s $^{-1}$  in the spectrum of the background QSO, SDSS J104257.58+074850.5. The absorption profile can be represented by a single Gaussian component with a FWHM of  $3.6 \pm 0.4$  km s $^{-1}$  shown on the spectrum. A second component ( $2.3 \sigma$ ) can be seen centered at  $9917.6$  km s $^{-1}$ . The properties of the absorber are consistent with that of a quiescent cloud that has a kinematic temperature of  $< 283$  K. *Bottom*: A comparison between the GBT spectrum and the VLBA spectrum of the 21 cm absorption feature. The GBT spectrum is binned to match the resolution of the VLBA spectrum. There is a good match between the two spectra for the primary component, i.e. towards the higher velocity-end of the feature. However, the VLBA spectrum shows a much stronger second component ( $4.6 \sigma$ ) as compared to the GBT spectrum.

. However, most of the data were uncorrupted on smaller velocity scales except for a few scans which showed strong interference features. The final spectrum, shown in Figure 7 and 8, was obtained by adding the uncorrupted data from our two observing sessions using the NRAO software GBTIDL. The rms noise in the final spectrum is 4.2 mJy. We clearly detect 21cm absorption at  $9924$  km s $^{-1}$ , i.e., very close to the optical redshift ( $H\alpha$ ) of the foreground galaxy, as we discuss in § 5.1. We note that the GBT data are corrupted by an RFI feature at  $\approx 9880$  km s $^{-1}$ , so any absorption/emission near that velocity could be difficult to detect, and in some regards it is more effective to use the VLA or VLBA data to search for features there.

#### 4.2. Very Large Array Observations

SDSS J104257.58+074850.5 was observed for two hours with the VLA in B-configuration on June 30, 2006 (project ID AT330). Only 22 antennas were available

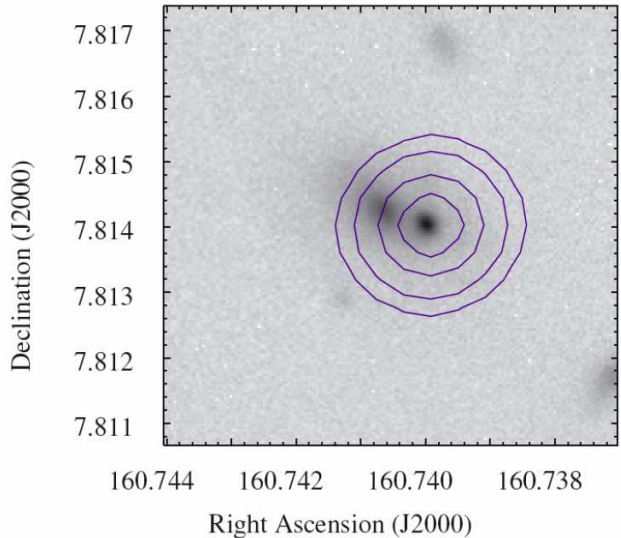


FIG. 9.— The VLA B-array 1.4 GHz continuum image of SDSS J104257.58+074850.5(contours) overplotted on the SOAR  $i$ -band image (grayscale). The resolution achieved in this image is  $6''$ . The contours are plotted at 50, 100, 200, 300, and 380 mJy/beam. The quasar is unresolved, and the extent of the contours reflects the VLA beam size in this configuration.

because of the Expanded VLA (EVLA) conversion that was occurring at the time. The correlator was configured in the single polarization 2IF mode with 64 spectral channels at a frequency resolution of 48.8 kHz ( $\sim 10.6$  km s $^{-1}$ ) per channel to cover a total bandwidth of 3.125 MHz ( $\sim 650$  km s $^{-1}$ ). The data were calibrated following the standard VLA calibration and imaging procedure in the Astronomical Image Processing Software (AIPS). Absolute uncertainty in the resulting flux density scaling is about 15%, and this is the formal uncertainty we quote for all physical parameters derived from the flux density.

We show in Figure 9 the 1.4 GHz continuum image from the VLA (contours) overplotted on the SOAR  $i$ -band image (grayscale). In this figure, the synthesized beam produced using natural weighting is  $5.8'' \times 5.5''$  (PA= $-73^\circ$ ). The 1.4 GHz continuum image shows a compact source, which is unresolved by the VLA, centered at  $\alpha(J2000) = 10^h 42^m 41.58^s$  and  $\delta(J2000) = +07^d 48^m 58.50^s$  with a peak flux density of  $395 \pm 59$  mJy.<sup>3</sup> This is about 3% larger than the 1.4 GHz flux density of the same source found in the archival VLA FIRST Survey (Becker et al. 1995). However, this difference is well within the absolute calibration uncertainty of the VLA. The unresolved radio source is centered on the QSO and is clearly offset from the center of the foreground galaxy by  $2.5''$  to the southwest.

The continuum-subtracted VLA H I spectrum of SDSS J104257.58+074850.5 covering the velocity range between  $9820$  km s $^{-1}$  and  $10150$  km s $^{-1}$  is shown in Figure 7. The rms noise in each  $10.6$  km s $^{-1}$  channel maps is  $\sim 0.7$  mJy beam $^{-1}$  (21 K), and no H I is significantly detected in emission. The narrow absorption feature seen at  $V = 9924$  km s $^{-1}$  is spectrally unresolved with an average optical depth of  $\tau_{\text{H I}} = 0.0101 \pm 0.0018$  ( $5.6\sigma$ ) over the  $10.6$  km s $^{-1}$  channel width.

<sup>3</sup> The  $1\sigma$  noise in the continuum image is about  $0.2$  mJy beam $^{-1}$ , which reflects the dynamic range of the data rather than thermal noise.

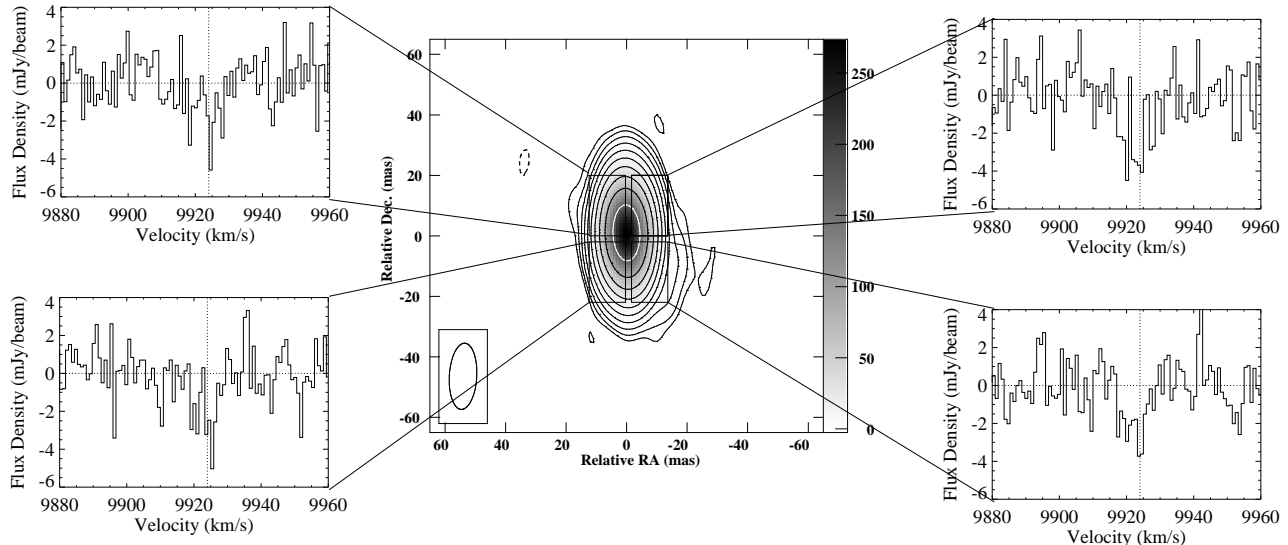


FIG. 10.— *Center panel*: The VLA 21 cm continuum image of the radio-bright quasar SDSS J104257.58+074850.5 (grayscale and contours). The continuum emission contours are plotted in linear increments of -4, 4 8, 16, 32, 64, 128, 256, 512, 1024, and 2048 of the rms flux of  $80 \mu\text{Jy}/\text{beam}$ , and the grayscale follows the scale bar on the right side of the central panel; the beam size and orientation are shown in the inset. The quasar is modestly resolved with peak and integrated flux densities of  $272 (\pm 0.1) \text{ mJy}/\text{beam}$  and  $341 (\pm 0.2) \text{ mJy}$ , respectively. *Side panels*: H I 21 cm absorption spectra from the foreground galaxy GQ1042+0747 extracted from the four independent regions to the background quasar indicated with boxes overlaid on the continuum image. Each H I 21 cm absorption panel is connected to the box indicating the region from which it was extracted. For purposes of comparison, all of the spectral plots are plotted with the same axis scales, and the velocity  $9924 \text{ km s}^{-1}$  is marked for reference (the optical redshift of the foreground galaxy is  $9932 \pm 10 \text{ km s}^{-1}$ ).

### 4.3. Very Long Baseline Array Observations

The VLBA observations of this source were carried out in two 8-hour observing sessions on the nights of 15 and 16 June 2008 under program ID BY124. Four adjacent 4 MHz baseband channel pairs were used in the observations, with both right and left hand circular polarization, and sampled at 2 bits. The data were correlated at the VLBA correlator in Socorro, New Mexico in two passes. In the first pass, all the baseband channels were correlated with 32 spectral channels per 4 MHz for the purpose of imaging the radio continuum emission. The second correlation pass was performed only on the second pair of baseband channels, which were centered at  $9925 \text{ km s}^{-1}$ . This produced a data cube with 1024 spectral channels and a resolution of  $3.9 \text{ kHz}$  ( $0.9 \text{ km s}^{-1}$ ) per channel. The total on-source integration time was 15 hours. Two of the 10 VLBA antennas were rendered unusable due to technical problems (Brewster) and data corruption (Mauna Kea). The data reduction was performed using AIPS.

After a priori flagging of data affected by interference in both data sets, amplitude calibration was performed using the measurements of the antenna gains and the system temperatures for each station. Bandpass calibration was performed using 3C 273. The continuum data set was then self-calibrated and imaged in an iterative cycle. Figure 10 shows the continuum image of the background quasar SDSS J104257.58+074850.5 that was obtained using an intermediate grid weighting between pure natural and pure uniform (Robust=2) in the IMAGR routine of AIPS. The angular resolution of this image is  $21.9 \text{ mas} \times 9.1 \text{ mas}$  (P.A. =  $3^\circ$ ) and the rms noise is  $80 \mu\text{Jy}/\text{beam}$ . At this resolution the source is resolved with peak and integrated flux densities of  $272.0 (\pm 0.1) \text{ mJy}/\text{beam}$  and  $341.0 (\pm 0.2) \text{ mJy}$ , respectively. The spatial extent of the

continuum source was fitted with a Gaussian profile that gave a nominal deconvolved size of  $8.5 \text{ mas} \times 2.4 \text{ mas}$  at FWHM. The radio emission associated with the QSO is core-dominated with an extension toward the southwest side of the core indicative of a weak jet-like feature. The visibility amplitude decreases to 50% of the peak at baseline length of  $\sim 10$  mega lambda, thus confirming the spatial extension of the QSO. The integrated flux measured in our VLBA image was  $40.6 \text{ mJy}$  less than that of the FIRST VLA survey, which suggests the presence of faint extended structure that was detected by the VLA but was resolved out by the VLBA.

The self-calibration solutions of the continuum data set were applied to the spectral line data cube, which was then imaged using a similar weighting as the continuum. The continuum emission was then subtracted from the H I cube. The bottom panel of Figure 7 shows the unsmoothed VLBA 21 cm H I spectrum from pixels with at least  $400 \mu\text{Jy}$  ( $5 \sigma$ ) continuum flux. The rms noise in the VLBA spectrum is  $2 \text{ mJy}/\text{beam}$ . Again, absorption near the redshift of GQ1042+0747 is readily apparent. A comparison of the VLBA and the GBT spectra binned at the same resolution is shown in the lower panel of Figure 8. To estimate the column density, we included channels within the velocity range  $9913$  to  $9930 \text{ km s}^{-1}$ . In order to minimize the effect of noise in the optical depth cube and the column density measurement, we blanked (removed) the pixels where the continuum emission was less than  $100 \text{ mJy}$ .

## 5. 21 CM MEASUREMENTS

### 5.1. 21 cm Component Structure and Kinematics

As shown in Figure 7, the H I 21 cm absorber in the foreground of SDSS J104257.58+074850.5 is confirmed by our observations using the GBT, the VLA, and the VLBA. While the GBT spectra provide the highest

spectral resolution, the VLBA imaging complements the GBT data by providing high angular resolution. Independent observations with the three telescopes are also helpful for overcoming systematic problems specific to one facility, e.g., the RFI problem at  $v \approx 9880 \text{ km s}^{-1}$  in the GBT data.

The H I absorber detected by the GBT has a primary component consistent with a single Gaussian profile with a centroid at  $9923.97 \pm 0.17 \text{ km s}^{-1}$  or  $1374.8923 \pm 0.0007 \text{ MHz}$  ( $z_{\text{abs}} = 0.033103$ ) and a FWHM of  $3.6 \pm 0.4 \text{ km s}^{-1}$ . A weaker component ( $\sim 2.3 \sigma$ ) can be seen at  $9917.6 \text{ km s}^{-1}$ . Close inspection of Figure 8 reveals a possible third component at  $\approx 9927 \text{ km s}^{-1}$ , but the significance of this third feature is marginal. Figure 8 shows the fit of a single Gaussian profile to the primary component of the H I absorption in the continuum subtracted GBT spectrum. The width of the Gaussian could be slightly overestimated due to blending with the tentative third component at  $9927 \text{ km s}^{-1}$ . Given the marginal significance of the third component, we have elected to fit the main component as shown in Figure 8 so that our line width places a conservative upper limit on the kinetic temperature of the absorbing gas (see §5.3). The bottom panel of Figure 8 shows a comparison of the GBT and the VLBA spectra. The profiles show similar peak absorption flux and line shapes for the primary component. However, the second component is much more prominent ( $4.6 \sigma$ ) in the VLBA spectrum and is slight shifted in velocity ( $v=9920 \text{ km s}^{-1}$ ).

The redshift measured from our highest resolution GBT H I data is  $\sim 8 \text{ km s}^{-1}$  lower than the redshift derived from the H $\alpha$  data, but is well within the uncertainty. In principle, the optical redshift could represent the systemic redshift of the galaxy. However, all of our optical spectra (from SDSS and APO) that detect the foreground galaxy emission lines are measured at the position of the QSO. As we can see from Figures 2 and 3, this position is offset from the galaxy center, and it is likely that at this location, the H II regions that produce the optical emission lines are rotating with the disk of the galaxy. The good agreement of the optical and 21cm redshifts suggests that the 21cm absorption arises in the disk and is corotating with the H II regions and the disk. The kinematical quiescence of the 21cm-absorbing gas warrants comment – as discussed in § 1, high- $z$  DLAs and sub-DLAs (e.g., Meiring et al. 2009) are noted for complex gas kinematics, which likely plays an important role in how the DLAs evolve. The 21cm absorption traces the *neutral* gas, and we see no evidence of complex kinematics in the neutral gas along our sight line through GQ1042+0747. We are likely detecting an ordinary gas cloud in the disk of the galaxy.

### 5.2. Spatial Variability of the 21 cm Absorption

One of the broad goals of this project is to investigate the transverse spatial distribution of the absorbing gas by taking advantage of the extended nature of QSOs at radio frequencies. For this purpose, Figures 10, 11, and 12 provide more detailed presentations of the spatial structure of the 21 cm absorption. Figure 10 shows the high resolution VLBA continuum image of the background QSO along with H I absorption spectra extracted from four different regions – Northwest, Northeast, Southwest, and Southeast. Each region is roughly the size of

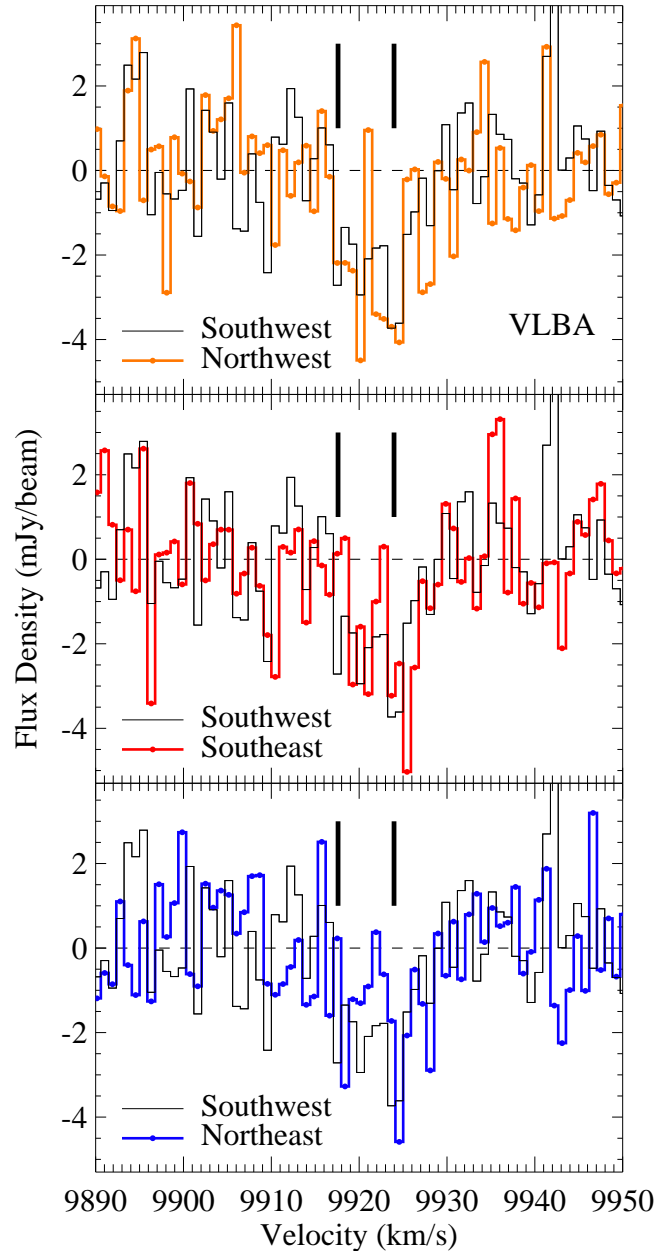


FIG. 11.— Direct comparison of the continuum-subtracted VLBA 21cm absorption profiles extracted from the four regions shown in Figure 10. *Top*: Absorption profile from the Southwest region (thin black line) overplotted on the profile from the Northwest region (thick orange line). *Middle*: Absorption profile from the Southwest region (thin black line) overplotted on the profile from the Southeast region (thick green line). *Bottom*: Absorption profile from the Southwest region (thin black line) overplotted on the profile from the Northwest region (thick blue line). In each panel, the thick black vertical lines above the spectra indicate the velocity centroids of the two components detected with the GBT.

the synthesized beams. To facilitate detailed comparisons, Figure 11 overplots the spectra from the Northwest, Northeast, and Southeast regions on top of the spectrum from the Southwest region. From these comparisons, we notice the following trends: First, as the regions move from West to East, the peak absorption flux in the main component increases and the velocity centroids shift to slightly higher velocities. Second, the

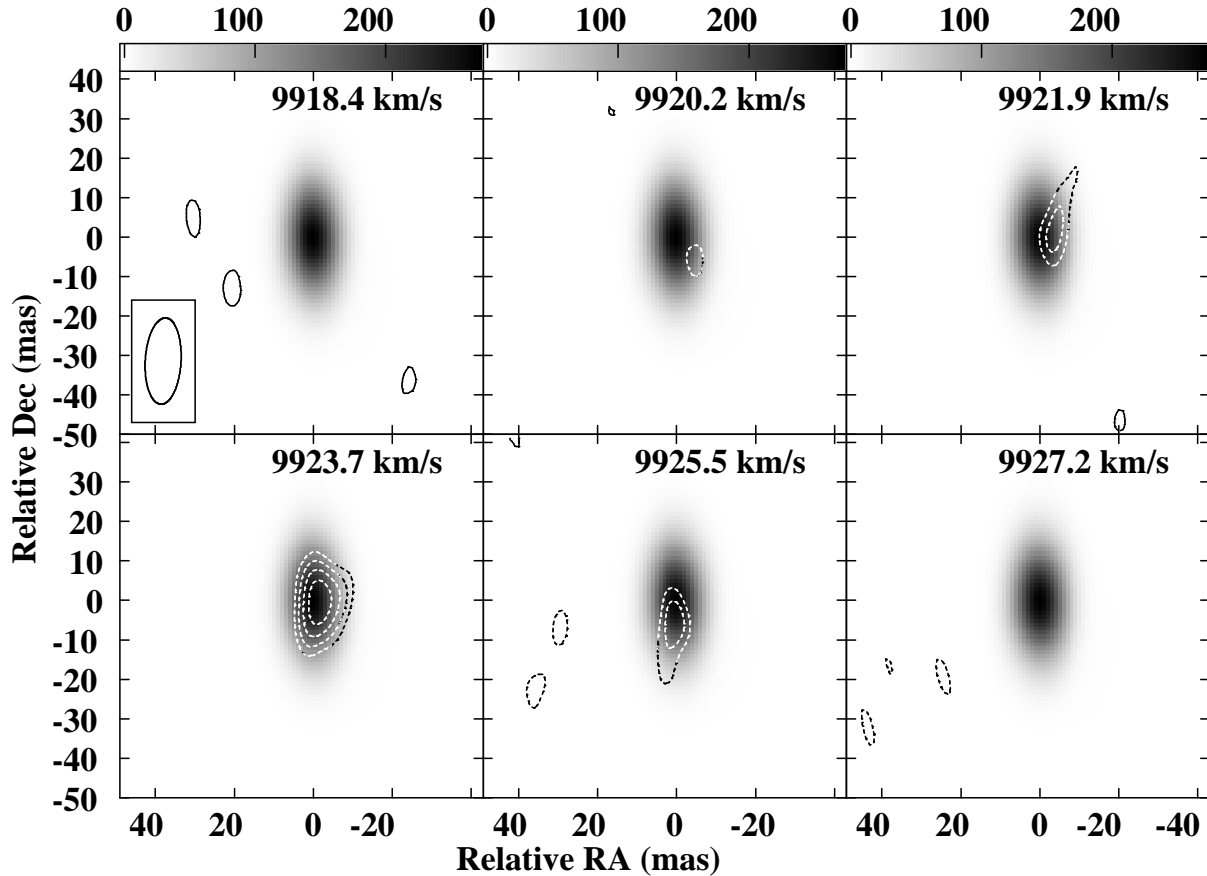


FIG. 12.— The VLBA 21 cm H I absorption from GQ1042+0747 (contours) superimposed on the VLBA 21cm continuum image (greyscale with the scalebars at top) of the background quasar SDSS J104257.58+074850.5 in velocity channel maps extending over the velocity range of the absorption detected in the GBT spectrum. The central velocity is indicated in each panel, and the beam characteristics are shown in the inset at upper left. To enhance the signal, two VLBA channels have been combined in each panel. The contours are plotted in linear increments of 3, 4, 5 and 6 times the rms noise of 1.5 mJy/beam.

weaker component (at  $v \approx 9920 \text{ km s}^{-1}$ ) is evident in all of the VLBA regions with its maximum strength in the West ( $3.1 \sigma$  in the Southeast and Southwest) and weakest in the Northeast ( $1.8 \sigma$ ). Both components appear to be narrower on the Eastern side, but this could be simply due to more blending on the Western side if the velocity centroids of the two components are shifting closer together in the West. The spatial variation in the strength of the absorber for each spectral channel is shown in Figure 12 where the absorption feature contours are superposed on the continuum image shown in grey scale. Each velocity plane is independent and the noise should not correlate between the images.

In the main component, the absorber covers most of the background quasar at the resolution of the VLBA imaging. The extent of the HI cloud as measured from the region with at least  $4 \sigma$  HI detection is  $41 \text{ mas} \times 21 \text{ mas}$  on the plane of the sky, which cor-

responds to a physical size of  $27.1 \text{ pc} \times 13.9 \text{ pc}$  at the redshift of the absorber. The similarity in peak absorption flux between the GBT and VLBA profiles suggest that the absorption is associated with the same absorber. Since the GBT beam is much larger, it is possible that the GBT spectrum includes absorption from an entirely different cloud than the gas that imprints the absorption on the VLBA spectrum. However, we would intuitively expect a separate and independent cloud to have different kinematics, which in turn would cause the GBT absorption profile to have a different shape from the VLBA absorption. Also, in this case, since the QSO is not very extended (the VLBA flux density is just  $\approx 40 \text{ mJy}$  lower than the flux from VLA FIRST Survey) and the absorber is very narrow, it is unlikely that there are multiple clouds associated with the absorber.

### 5.3. Kinetic Temperature of the H I 21 cm Absorber

Interstellar neutral gas in disk galaxies is believed to be distributed in two distinct physical phases - the warm neutral medium (WNM) and the cold neutral medium (CNM). While the WNM is diffuse and has a temperature in the range of 5000 to 8000 K, the CNM exists as clumpy dense clouds with temperatures in the range of 20 to 250 K (Kulkarni & Heiles 1988). This has been confirmed in numerous extragalactic studies including Young & Lo (1997a,b), Carilli et al. (1998), and Lane et al. (2000).

The width of an absorption line can be used to derive an upper limit on the kinetic temperature of the gas, assuming the line width is predominantly due to thermal broadening (this is an upper limit because other factors, e.g., turbulence, can also broaden the line). For neutral hydrogen, the kinetic temperature upper limit can be estimated using

$$T_k \leq 21.855(\Delta v)^2 \quad (6)$$

where  $\Delta v$  is the FWHM velocity in  $\text{km s}^{-1}$ . Based on the Gaussian fitting from our high resolution GBT data, we estimate that the FWHM of the absorption feature is  $3.6 \text{ km s}^{-1}$ , which indicates that

$$T_k \leq 283 \text{ K}. \quad (7)$$

Thus, the temperature suggests that the 21cm absorption arises in the CNM of GQ1042+0747.

#### 5.4. H I Column Density and Volume Density

With the temperature constraint afforded by the high spectral resolution of the data, the H I column density can be estimated by integrating over the 21 cm absorption profile using the standard equation (e.g., Rohlfs 1986):

$$N(\text{H I}) = 1.823 \times 10^{18} \frac{T_s}{f} \int \tau_{21}(v) dv, \quad (8)$$

where  $T_s$  is the spin temperature,  $f$  is the fraction of the radio flux source that is covered by the absorbing gas and is assumed to be unity, and  $\tau_{21}(v)$  is the 21 cm optical depth in velocity space (in  $\text{km s}^{-1}$ ). In the GBT spectra the peak optical depth was measured to be  $0.076 \pm 0.011$ . Given the context of the absorption (i.e., arising in the disk of a spiral galaxy), it is likely that the density is high enough so that the level populations of the H I hyperfine structure levels are set predominantly by collisions. Thus we can assume that  $T_s \approx T_k$ . With  $T_k \leq 283 \text{ K}$  (§5.3), we obtain

$$N(\text{H I})_{\text{GBT}} \leq 9.6 \times 10^{19} \text{ cm}^{-2} \quad (9)$$

by integrating over the main absorption line detected with the GBT. This indicates that the 21cm absorber is not quite a damped Lyman  $\alpha$  absorber according to the usual definition. This is somewhat surprising given the small impact parameter of the sight line to an actively star-forming spiral galaxy. We discuss this further in § 6. However, if we apply the same procedure to the VLBA data to extract the overall H I profile for pixels with continuum flux  $\geq 100 \text{ mJy}$ , we obtain

$$N(\text{H I})_{\text{VLBA}} \leq 1.5 \times 10^{20} \text{ cm}^{-2}. \quad (10)$$

The difference between the GBT and the VLBA column density constraints could result from a difference in the covering fraction ( $f$ ) between the two observations. Since

the VLBA resolves out the source, the angular extent of the continuum source could be smaller for the VLBA than the GBT, so although the covering fraction estimated from the VLBA observations is  $\sim 1$ , the covering fraction for the GBT observations could be lower than 1. We note from Figure 11 that while the VLBA centroids of the main absorption component (at  $v \approx 9924 \text{ km s}^{-1}$ ) match up well with the centroid of that component indicated by the GBT data, the GBT centroid of the weaker feature (at  $9917.6 \text{ km s}^{-1}$ ) is slightly offset to shorter velocities compared to the velocity of that component in the VLBA spectra. This could also be an indication that some of the GBT absorption at  $9917.6 \text{ km s}^{-1}$  occurs outside the continuum region detected by the VLBA.

In §5.2, we showed that there is some subtle spatial variability of the 21cm absorption, but overall, similar absorption is detected in all directions probed with the VLBA data. This indicates that the dimensions of the absorbing cloud are at least  $27.1 \text{ pc} \times 13.9 \text{ pc}$ . Assuming the cloud to be an ellipsoid that has a spin temperature of 283 K, the estimated H I mass limit for this cloud is  $356 M_\odot$ . If we take  $\approx 14 \text{ pc}$  as the minimum line-of-sight size of the cloud and combine this with the VLBA upper limit on  $N(\text{H I})$ , we find that the volume density of the gas is

$$n(\text{H I}) < 3.5 \text{ cm}^{-3}. \quad (11)$$

While the cloud size implied by the VLBA data is consistent with expectations for a CNM cloud, this upper limit on  $n(\text{H I})$  is an order of magnitude lower than expected for the CNM (cf., Jorgenson et al. 2009; Tielens 2005). It is worth noting that our density values are based on the assumption that the line-of-sight length of the absorbing cloud is 14 pc. Since the VLBA absorption region of  $27 \text{ pc} \times 14 \text{ pc}$  transverse to the sight line covers almost the entire continuum source with an extension in the Northwest-Southeast direction, it may be possible that the absorbing cloud extends beyond the region probed by the VLBA continuum data. Therefore, our size measurement is a limiting value and the line-of-sight length of 14 pc is a conservative lower limit. If the absorbing cloud is larger, then the implied number density is even lower, which further exacerbates the discrepancy with the typical density expected in CNM regions. Of course, it is possible that the cloud contains high-density internal clumps that are much smaller than the VLBA beam. In this case, the line-of-sight length could be lower and the density could be higher. However, in this situation we might expect to see more dramatic spatial variability in the VLBA absorption profiles. We do notice some weak variability in the VLBA profiles, but overall the four VLBA sight lines show the same basic profile shapes (see Figure 10). This suggests that the absorbing cloud extends across the entire region probed by the VLBA data. We have not estimated the effects of ISM scintillation and microlensing on the apparent size of the emitting region. Such assessment is beyond the scope of this discussion.

#### 5.5. Total H I Mass of GQ1042+0747

Our 21 cm spectra show no indication of H I emission associated with the foreground galaxy (see Figure 7). The absence of 21 cm emission provides an upper limit on the total H I mass of GQ1042+0747. Based on the GBT

noise properties and assuming a line-width of  $100 \text{ km s}^{-1}$ , we estimate a  $3\sigma$  H I mass limit of less than  $5.1 \times 10^8 M_{\odot}$  for the foreground galaxy. This is an order of magnitude less than the H I mass associated with a typical luminous spiral galaxy ( $L \sim L_{*}$ ). However, GQ1042+0747 has  $L \ll L_{*}$ , and this upper limit on  $M(\text{H I})$  is entirely consistent with the H I masses measured in dwarf galaxies (e.g., Matthews et al. 1995, 1996, 1998; Swaters et al. 2002; Begum et al. 2008). Our GBT data should provide the most stringent limits on  $M(\text{H I})$  for any narrow features with  $\Delta V \sim 100 \text{ km s}^{-1}$ . The GBT spectra suffered from sinusoidal standing waves as commonly found when observing bright continuum sources and consequently broad and faint features of the order  $\Delta V \geq 300 \text{ km s}^{-1}$  may have been missed. We also examined the ALFALFA data (private communication with R. Giovanelli) which show signs of a moderate enhancement from 9775 to 10078  $\text{km s}^{-1}$ . This corresponds to an H I mass of  $4.5 \times 10^9 M_{\odot}$ . However, the ALFALFA data also shows signs of sinusoidal modulations thus adding a significantly large uncertainty to the mass estimation. We plan to observe GQ1042+0747 with the Arecibo Telescope to correctly estimate its H I mass. The next section discusses the implications of the H I mass of GQ1042+0747 and compares the galaxy to H I emission from other dwarf galaxies.

## 6. DISCUSSION

### 6.1. H I Deficiency: Evidence of Gas Consumption in an Isolated Environment?

High-resolution H I surveys of dwarf and irregular galaxies such as the Westerbork observations of neutral Hydrogen in Irregular and SPiral galaxies (WHISP) Survey (Swaters et al. 2002) or the Faint Irregular Galaxy GMRT Survey (FIGGS) (Begum et al. 2008) generally find dwarf galaxies to have H I envelopes extending over much larger area than their optical disks. However, our radio observations of the QSO sight line that pierce the inner disk of GQ1042+0747 reveal that the galaxy is surprisingly H I-deficient in several ways. Although we detect a cold H I cloud in this galaxy, it is a sub-DLA at best, unlike what is expected from emission maps of similar galaxies from the WHISP and FIGGS surveys. Likewise, by combining the H I column density with constraints on the size of the absorbing cloud from the VLBA data, we find that  $n(\text{H I}) < 3.5 \text{ cm}^{-3}$ , which is roughly an order of magnitude lower than expected for a CNM cloud. Here, we attempt to understand if GQ1042+0747, which appears to be an ordinary dwarf spiral in optical imaging with ongoing star formation, is consistent with H I emission studies of dwarf galaxies or if GQ1042+0747 is a special case.

In order to understand the discrepancy between dwarf H I galaxies and GQ1042+0747, it is important to analyze any possible bias between our selection criterion and that of the above mentioned surveys. Since GQ1042+0747 was identified using optical emission lines, our selection criteria differ from those of WHISP and FIGGS, which are *H I -selected*, i.e., a criterion for including the galaxies in these surveys in the first place was that they were already known to have detectable H I emission. This could introduce a problematic bias when comparing their properties to GQ1042+0747. It is possible that galaxies such as GQ1042+0747 belong to a

different population of dwarf galaxies than the H I rich dwarfs commonly seen in H I surveys.

We believe the most appropriate way to understand the nature of GQ1042+0747 is to compare it with a dwarf galaxy sample which was not H I-selected. In a series of papers, Matthews and Gallagher surveyed the H I emission properties of a sample of faint “extreme late-type” galaxies selected to have no published H I information before their survey (e.g., Gallagher et al. 1995; Matthews et al. 1995, 1996). They found a range of modestly to highly gas-rich galaxies with H I masses and optical properties consistent with our constraints on GQ1042+0747. In a follow-up study of *isolated* extreme late-type galaxies, Matthews et al. (1998) argue that these galaxies are not “scaled-down” versions of luminous gas-rich galaxies. Instead, they find that the extreme late-type galaxies often form stars sluggishly compared to more luminous late-type galaxies.

These results of Matthews et al. (1998) suggest a possible class of dwarf galaxies with properties similar to GQ1042+0747. In §3.4, we showed that GQ1042+0747 is an isolated galaxy at the edge of a large-scale structure (see Figure 6). If this dwarf galaxy is forming stars relatively slowly like the extreme late-type galaxies of Matthews et al. (1998), it may be gradually consuming its gas reservoir without being replenished with fresh gas from its intergalactic surroundings or from interactions with other galaxies.

A variation of this hypothesis is that for some reason, this galaxy is not able to efficiently transport gas into the inner region probed by the SDSS J104257.58+074850.5 sight line so that the H I is depleted in its central regions thereby creating an H I gap/hole. Interestingly, similar H I gaps/holes have been reported in H I -selected dwarf galaxies such as DDO43 by Begum et al. (2008). In addition, close inspection of the WHISP H I maps reveals other galaxies with similar patchy H I distributions with lower H I intensities in some parts of their inner regions. It would be interesting to re-observe GQ1042+0747 galaxy with higher angular resolution with the upcoming Atacama Large Millimeter Array to explore the distribution and physical properties of the molecular gas. High-resolution *Hubble Space Telescope* (*HST*) imaging would also provide insight about the star-formation history in GQ1042+0747.

### 6.2. Quiescent Neutral Gas

Another possible explanation for the low amount of H I revealed by our observations is that gas in the central region of the galaxy has been partially evacuated by a galactic outflow, either a bound galactic fountain or an escaping galactic wind. Such outflows have been observed in nearby starburst galaxies (Veilleux et al. 2005, and references therein), and indications of a *bound* outflow have been seen in the central region of the Milky Way (e.g., Bland-Hawthorn & Cohen 2003; Keeney et al. 2006). It has long been known that there is a deficit of extraplanar H I in the inner 3 kpc of the Milky Way (Lockman 1984), which could be due to expulsion of H I from the inner Galaxy by some type of outflow (e.g., Everett et al. 2008).

If this type of outflow is driving gas out of the inner region of GQ1042+0747, then we might expect to see kinematical evidence of the outflowing gas (as was done



in, e.g., Keeney et al. 2006). However, contrary to the kinematics seen in the metal-line absorption profiles of many high- $z$  DLAs (e.g., Prochaska & Wolfe 1997), the 21 cm H I line profile of GQ1042+0747 is quite simple, and we see no indications of outflowing neutral gas. However, there are some caveats. We might not detect the outflowing neutral gas if the spin temperature is too high or the covering factor is low. Conversely, the kinematics of high- $z$  galaxies are often traced by species, such as Si II, that can exist in ionized gas as well as neutral gas, and it is possible that the complex kinematics of the high- $z$  systems could be partly due to ionized gas that we would not see in 21cm absorption. To test this possibility, it would be valuable to observe SDSS J104257.58+074850.5 in the ultraviolet with the Cosmic Origins Spectrograph (COS) on *HST*. Ultraviolet spectra provide sensitive probes of ionized gas, and the combination of the UV and 21cm data would provide a direct measurement of the spin temperature of the neutral gas. It is also plausible that a warm neutral medium (WNM) is present in this galaxy; if the WNM has a sufficiently large velocity dispersion and low optical depth, then such features could be lost in the process of baseline fitting. This can also be tested with COS observations using O I absorption lines, which are locked to the neutral gas by a resonant charge exchange reaction.

In § 1, we discussed the need to probe the signatures of neutral gas that exists in different contexts. Of course, this requires a sample that is large enough to support statistically significant conclusions, but it is interesting to note that if we make the reasonable assumption that  $T_k \approx T_s$  and we adopt the metallicity from the optical emission lines (Table 2), then we find that the spin temperature in GQ1042+0747 adheres to the spin temperature – metallicity relation recently presented by Kanekar et al. (2009b). They discuss several hypotheses for the cause of this correlation and conclude that the increase in the number of possible radiative pathways for cooling gas with an increase in metallicity is the likely cause. Extending their argument to the case of GQ1042+0747, it seems likely that the higher metallicity in the inner disk of GQ1042+0747 causes the gas to cool more rapidly. Many high- $z$  DLAs are known to have higher spin temperatures (Kanekar & Chengalur 2005). The high- $T_s$  absorbers could originate in outer disks (or tidal/dynamical debris) where the densities and metallicities are lower and the cooling times are longer. However, it is also possible that the cooling times are longer simply because high- $z$  galaxies have substantially lower metallicities. It would be interesting to place constraints on  $T_s$  in a sample of *nearby* galaxies probed at a range of impact parameters and with a range of galaxy properties.

## 7. SUMMARY AND CONCLUDING REMARKS

The SDSS presents a remarkable (and largely untapped) opportunity to study gas that is difficult to observe in low-redshift galaxies/galaxy groups by observing absorption imprinted on the spectra of quasars that happen to be located in the background of galaxies of interest. While the SDSS obtains spectra of these background quasars, the spectra have somewhat low resolution and sensitivity for absorption spectroscopy and only cover the optical band. Thus, while the SDSS provides an invaluable database for selecting background QSO - fore-

ground galaxy groupings for this type of study, follow-up observations with higher resolution instruments and in other frequency bands will be required to fully exploit the technique. To demonstrate the potential of SDSS for 21cm studies of this type, we have observed with the GBT, VLA, and VLBA the radio-loud quasar SDSS J104257.58+074850.5 that pierces a foreground star-forming spiral galaxy (GQ1042+0747) at a very small impact parameter. To complement the 21cm observations, we have also obtained images with the SOAR telescope (which provides better angular resolution than the SDSS imaging) and follow-up spectroscopy with the APO 3.5m telescope. From this suite of observations, we have obtained the following results:

1. The high-resolution optical imaging with SOAR shows that the foreground galaxy is a low-luminosity spiral galaxy, and the quasar sight line is at a projected distance of 2.5'' from the center of the foreground galaxy, which corresponds to an impact parameter of 1.7 kpc for our assumed cosmology. The emission lines of the foreground galaxy imply a SFR surface density of  $0.004 M_\odot \text{ yr}^{-1} \text{ kpc}^{-2}$  and a metallicity of  $-0.27 \pm 0.05$  dex relative to Solar. The optical  $H\alpha/H\beta$  ratio also indicates that the galaxy has a low dust content, at least in the region encompassed by the 3'' SDSS fiber ( $3.1 \text{ kpc}^2$ ) centered at the position of the background QSO. The galaxy colors indicate that its approximate stellar mass is  $M_{\text{stars}} \approx 10^{9.1} M_\odot$ .
2. Using larger-scale information about the distribution of galaxies in the vicinity of the foreground galaxy from the SDSS, we find that this object is a relatively isolated galaxy near the boundary of a large-scale structure.
3. The spectra obtained with the GBT, VLA, and VLBA independently reveal H I 21 cm absorption in the spectrum of the background QSO at the redshift of foreground galaxy. Two components separated by  $\approx 6 \text{ km s}^{-1}$  are evident in the GBT and VLBA spectra; a third feature may be present but is only recorded at marginal significance. However, it is clear that the absorption profiles indicate simple and quiescent kinematics. The high spectral resolution of the GBT data places a strong upper limit on the kinetic temperature of the 21cm-absorbing gas in the strongest component,  $T_k \leq 283 \text{ K}$ .
4. The background QSO is relatively compact, but nevertheless the VLBA observations resolve the continuum emission source and enable a preliminary search for small-scale spatial variability in the 21cm absorption arising in the foreground galaxy. We find variations in the optical depth and centroids of the 21cm absorption from four independent sight lines through GQ1042+0747 extracted from the VLBA data, but the variations are at a low level, and overall the absorption detected in the four regions shows similar optical depths and component structure. This indicates that the main absorbing cloud covers most of the continuum re-

gion detected with the VLBA and has dimensions of at least  $27.1 \text{ pc} \times 13.9 \text{ pc}$ .

5. Combining the upper limit on the kinetic temperature with the large covering factor indicated by the VLBA data, we obtain  $N(\text{H I}) < 9.6 \times 10^{19} \text{ cm}^{-2}$  from the GBT data and  $N(\text{H I}) < 1.5 \times 10^{20} \text{ cm}^{-2}$  from the VLBA data; the difference may be due to differences in the region probed by the large-beam single-dish telescope vs. the small-beam interferometer. The lower limit on the size of the main absorbing cloud combined with the VLBA  $N(\text{H I})$  constraint indicates that the H I volume density is less than  $3.5 \text{ cm}^{-3}$ .
6. We offer some remarks about the implications of our measurements. We suggest that GQ1042+0747 provides information about how the stars and gas in an isolated galaxy evolve if left largely undisturbed. It appears that the gas in the inner region of the galaxy is being depleted (compared to other spirals) by conversion to stars without being replenished with inflowing matter. It seems unlikely that an outflow is depleting the gas; we see no evidence of outflowing material, but further observations are required to properly search for such outflows. The galaxy follows the spin temperature – metallicity relation seen in higher-redshift DLAs.

The present understanding of H I clouds and their characteristics on parsec scales outside our own galaxy is quite limited. This is pathfinding work for future 21 cm absorber investigations. With upcoming facilities like the EVLA providing higher spectral resolution, larger bandwidth, and smaller beam size, 21cm absorbers will likely be detected in galaxies toward background QSOs much more efficiently. Moreover, RFI environment for EVLA is expected to be different from single-dish instruments, which may be very helpful in cases affected by local RFIs. This will enable detailed studies of the nature and distribution of cold gas in galaxies at different distances from the disk. This is also a useful technique for assembling a DLA/sub-DLA sample for future UV and/or optical spectroscopic studies that is not metallicity biased. Combining our understanding of the cold component traced by 21 cm H I absorbers with the warmer component traced by Lyman  $\alpha$  and metal absorbers will be valuable for understanding the nature, physical conditions, dynamics, and the role of neutral clouds in galaxy evolution.

This research has benefited from discussions with D. Calzetti, J. Gallagher, R. Giovannelli, D. Keres, S. Stanimirović, J. Stocke, and J. van Gorkom. The authors are grateful to the observatory staff at the GBT, the VLA and the VLBA who made these observations possible. SB is grateful for a Student Observing Support award (GSSP08-0024) from the National Radio Astronomy Observatory that made this work possible. SB and TMT also acknowledge financial support for this research from NASA grant NNX08AJ44G. D.V.B is funded through NASA LTSA grant NNG05GE26G. Funding for the SDSS and SDSS-II has been provided by the Alfred P. Sloan Foundation, the Participating Institutions, the

National Science Foundation, the U.S. Department of Energy, the National Aeronautics and Space Administration, the Japanese Monbukagakusho, the Max Planck Society, and the Higher Education Funding Council for England. The SDSS Web Site is <http://www.sdss.org/>. The SDSS is managed by the Astrophysical Research Consortium for the Participating Institutions. The Participating Institutions are the American Museum of Natural History, Astrophysical Institute Potsdam, University of Basel, University of Cambridge, Case Western Reserve University, University of Chicago, Drexel University, Fermilab, the Institute for Advanced Study, the Japan Participation Group, Johns Hopkins University, the Joint Institute for Nuclear Astrophysics, the Kavli Institute for Particle Astrophysics and Cosmology, the Korean Scientist Group, the Chinese Academy of Sciences (LAMOST), Los Alamos National Laboratory, the Max-Planck-Institute for Astronomy (MPIA), the Max-Planck-Institute for Astrophysics (MPA), New Mexico State University, Ohio State University, University of Pittsburgh, University of Portsmouth, Princeton University, the United States Naval Observatory, and the University of Washington. The SOAR Telescope is a joint project of: Conselho Nacional de Pesquisas Cientificas e Tecnológicas CNPq-Brazil, The University of North Carolina at Chapel Hill, Michigan State University, and the National Optical Astronomy Observatory.

*Facilities:* ARC (), GBT (), Sloan (), VLA (), VLBA ()

## REFERENCES

- Asplund, M., Grevesse, N., Sauval, A. J., & Scott, P. 2009, *ARA&A*, 47, 481
- Becker, R. H., White, R. L., & Helfand, D. J. 1995, *ApJ*, 450, 559
- Begum, A., Chengalur, J. N., Karachentsev, I. D., Sharina, M. E., & Kaisin, S. S. 2008, *MNRAS*, 386, 1667
- Bell, E. F., McIntosh, D. H., Katz, N., & Weinberg, M. D. 2003, *ApJS*, 149, 289
- Bergeron J., & Boisse P. 1991, *A&A*, 243, 344
- Bertin, E. & Arnouts, S. 1996, *A&AS*, 117, 393B
- Bland-Hawthorn, J., & Cohen, M. 2003, *ApJ*, 582, 246
- Blanton, M. R. et al. 2003, *ApJ*, 592, 819B
- Blanton, M. R. et al. 2005, *AJ*, 129, 2562
- Bowen, D. V., Tripp, T. M., & Jenkins, E. B. 2001, *AJ*, 121, 1456B
- Carilli, C. L., Dwarakanath, K. S., & Goss, W. M. 1998, *ApJ*, 502, 79C
- Chen H.-W., Lanzetta K. M. 2003, *ApJ*, 597, 706
- Condon, J. J., Cotton, W. D., Greisen, E. W., Yin, Q. F., Perley, R. A., Taylor, G. B., & Broderick, J. J. 1998, *AJ*, 115, 1693
- Curran, S. J., Tzanavaris, P., Pihlström, Y. M., & Webb, J. K. 2007, *MNRAS*, 382, 1331
- Ellison, S. L., York, B. A., Murphy, M. T., Zych, B. J., Smith, A. M., & Sarre, P. J. 2008, *MNRAS*, 383, L30
- Ellison, S. L., & Lopez, S. 2009, *MNRAS*, 397, 467
- Everett, J. E., Zweibel, E. G., Benjamin, R. A., McCammon, D., Rocks, L., & Gallagher, J. S. 2008, *ApJ*, 674, 258
- Gallagher, J. S., Littleton, J. E., & Matthews, L. D. 1995, *AJ*, 109, 2003
- Gupta, N., Srianand, R., Petitjean, P., Noterdaeme, P., & Saikia, D. J. 2009, *MNRAS*, 398, 201
- Hibbard, J. E., van Gorkom, J. H., Rupen, M. P., & Schiminovich, D. 2001, in *Gas and Galaxy Evolution*, ASP Conf. Series 240, eds. J. E. Hibbard, J. H. van Gorkom, & M. P. Rupen, (San Francisco: ASP), 657
- Jedrzejewski, R. I. 1987, *MNRAS*, 226, 747
- Jenkins, E. B., Bowen, D. V., Tripp, T. M., & Sembach, K. R. 2005 *ApJ*, 623, 767
- Jorgenson, R. A., Wolfe, A. M., Prochaska, J. X., & Carswell, R. F. 2009, *ApJ*, 704, 247
- Junkkarinen, V. T., Cohen, R. D., Beaver, E. A., Burbidge, E. M., Lyons, R. W., & Madejski, G. 2004, *ApJ*, 614, 658
- Kanekar, N., & Briggs, F. H. 2004, *NewAR*, 48, 1259
- Kanekar, N., & Chengalur, J. N. 2005, in *Probing Galaxies Through Quasar Absorption Lines*, IAU Colloquium 199, eds. P. R. Williams, C. Shu, & B. Ménard, (Cambridge: Cambridge University Press), p.156
- Keeney, B. A., Momjian, E., Stocke, J. T., Carilli, C. L., & Tumlinson, J., 2005, *ApJ*, 622, 267
- Keeney, B. A., Danforth, C. W., Stocke, J. T., Penton, S. V., & Shull, J. M. 2006, *ApJ*, 646, 951
- Kanekar, N., Prochaska, J. X., Ellison, S. L., & Chengalur, J. N. 2009a, *MNRAS*, 396, 385
- Kanekar, N., Smette, A., Briggs, F. H., & Chengalur, J. N. 2009b, *ApJ*, 705, L40
- Kennicutt R. C. Jr. 1998, *ARA&A*, 36, 189
- Kewley L. J., Geller M. J., & Jansen R. A. 2004, *AJ*, 127, 2002
- Kulkarni, S. R., & Heiles, C. 1988, in *Galactic and extragalactic radio astronomy*, 2nd edition, Springer-Verlag, 95-153.
- Lane, W. M., Briggs, F. H., & Smette, A. 2000, *ApJ*, 532, 146L
- Lazio, T. J. W., Brogan, C. L., Goss, W. M., & Stanimirović, S. 2009, *AJ*, 137, 4526
- Le Brun V., Bergeron J., Boisse P., Deharveng J. M. 1997, *A&A*, 321, 733
- Lockman, F. J. 1984, *ApJ*, 283, 90
- Lundgren, B. F., et al. 2009, *ApJ*, 698, 819
- Lupton, R., Blanton, M. R., Fekete, G., Hogg, D. W., O'Mullane, W., Szalay, A., & Wherry, N. 2004, *PASP*, 116, 133L
- McIntosh, D. H., Guo, Y., Hertzberg, J., Katz, N., Mo, H. J., van den Bosch, F. C., & Yang, X. 2008, *MNRAS*, 388, 1537
- Macdonald, E., Darling, J., ALFALFA Team et al. 2009, *BAAS*, 41, 451
- Matthews, L. D., Gallagher, J. S., & Littleton, J. E. 1995, *AJ*, 110, 581
- Matthews, L. D., & Gallagher, J. S. 1996, *AJ*, 111, 1098
- Matthews, L. D., van Driel, W., & Gallagher, J. S. 1998, *AJ*, 116, 1169
- Meiring, J. D., Kulkarni, V. P., Lauroesch, J. T., Péroux, C., Khare, P., & York, D. G. 2009, *MNRAS*, 393, 1513M
- Noterdaeme, P., Petitjean, P., Ledoux, C., & Srianand, R. 2009a, *A&A*, 505, 1087
- Noterdaeme, P., Srianand, R., & Mohan, V. 2009b, arXiv:0912.0736
- Péroux, C., Storrie-Lombardi, L. J., McMahon, R. G., Irwin, M., & Hook, I. M. 2001, *AJ*, 121, 1799P
- Pettini, M., & Pagel, B. E. J. 2004, *MNRAS*, 348, L59
- Pettini, M., Zych, B. J., Steidel, C. C., & Chaffee, F. H. 2008, *MNRAS*, 385, 2011
- Pontzen, A., Governato, F., Pettini, M. et al. 2008, *MNRAS*, 390, 1349
- Prochaska, J. X., & Wolfe, A. M. 1997, *ApJ*, 487, 73
- Prochaska, J. X., Howk, J. C., & Wolfe, A. M. 2003, *Nature*, 423, 57
- Prochaska, J. X., Herbert-Fort, S., & Wolfe, A. M. 2005, *ApJ*, 635, 123P
- Prochaska, J. X., Chen, H.-W., Wolfe, A. M., Dessauges-Zavadsky, M. & Bloom, J. S. 2008, *ApJ*, 672, 59
- Prochaska, J. X., & Wolfe, A. M. 2009, *ApJ*, 696, 1543
- Quashnock, J. M., Kuttruff, S., Bishof, M. et al. 2008, *BAAS*, 212, 2603
- Rao S., Nestor D. B., Turnshek D., Lane W. M., Monier E. M., Bergeron J. 2003, *ApJ*, 595, 94
- Razoumov, A. O., Norman, M. L., Prochaska, J. X., Sommer-Larsen, J., Wolfe, A. M., & Yang, Y.-J. 2008, *ApJ*, 683, 149
- Rohlfs, K. & Wilson, T., 2000, *Tools of Radio Astronomy*, 3rd Edition (Berlin: Springer-Verlag), p305
- Schlegel, D. J., Finkbeiner, D. P., & Davis, M. 1998, *ApJ*, 500, 525S
- Schwarz, H. E., Ashe, M. C., Boccas, M. et al. 2004, *SPIE*, 5492, 564
- Steidel, C. C., Bowen, D. V., Blades, J. C., & Dickinson, M. 1995, *ApJ*, 440, 45
- Stocke, J. T., Case, J., Donahue, M., Shull, J. M., & Snow, T. P. 1991, *ApJ*, 374, 72
- Swaters, R. A., van Albada, T. S., van der Hulst, J. M., & Sancisi, R. 2002, *A&A*, 390, 829
- Tielens, A. G. G. M. 2005, *The Physics and Chemistry of the Interstellar Medium*, (Cambridge: Cambridge University Press)
- Tremonti, C. A., et al. 2004, *ApJ*, 613, 898
- Turnshek, D. A., Rao, S., Nestor, D., Lane, W., Monier, E., Bergeron, J., & Smette, A. 2001, *ApJ*, 553, 288
- Veilleux, S., Cecil, G., & Bland-Hawthorn, J. 2005, *ARA&A*, 43, 769
- Wolfe, A. M., & Turnshek, D. A., Smith, H. E., & Cohen, R. D. 1986, *ApJS*, 61, 249
- York, B. A., Ellison, S. L., Lawton, B., Churchill, C. W., Snow, T. P., Johnson, R. A., & Ryan, S. G. 2006a, *ApJ*, 647, L29
- York, D. G., et al. 2000, *AJ*, 120, 1579
- York, D. G., et al. 2006b, *MNRAS*, 367, 945.
- Young, L. M., & Lo, K. Y. 1997a, *ApJ*, 476, 127Y
- Young, L. M., & Lo, K. Y. 1997b, *ApJ*, 490, 710Y